공학박사 학위논문

Plasma Current and Pressure Profile Effects on Tearing Mode Onset in Steady-state Hybrid Scenarios on DIII-D Tokamak

DIII-D 정상상태 하이브리드 운전에서의 플라즈마 전류 및 압력 분포 변화에 따른 찢어짐 모드 발생 안정성 평가

2017 년 2 월

서울대학교 대학원
에너지시스템공학부
김 경 진

Plasma Current and Pressure Profile Effects on Tearing Mode Onset in Steady-state Hybrid Scenarios on DIII-D Tokamak

by

Kyungjin Kim

Advisor : Professor Yong-Su Na, Ph.D.

Submitted in Partial Fulfillment of the Requirements

for the Degree of Doctor of Philosophy

in Seoul National University

February, 2017

Department of Energy System Engineering

Graduate School

Seoul National University

ABSTRACT

Plasma Current and Pressure Profile Effects on Tearing Mode Onset in Steady-state Hybrid Scenarios on DIII-D Tokamak

Kyungjin Kim
Department of Energy System Engineering
The Graduate School
Seoul National University

Tearing mode (TM) instability is a kind of resistive magnetohydrodynamic instability that limits the performance of the tokamak plasma. A correct understanding of this phenomenon is essential for high performance steady-state operation, especially the onset of TMs. Based on the steady-state hybrid experiments performed on the DIII-D device, the occurrence of TM is identified and analyzed, and the effect of the plasma current and the pressure profiles on the tearing stability is investigated in terms of the tearing stability index Δ'.

The characteristics of the mode is mainly investigated using the system of

magnetic pick-up Mirnov probes. The FFT analysis and the phase-fitting method are applied to identify the mode onset, the mode amplitude, and the mode number in the experiments. The mode onset was defined for this thesis that the phase-folding disappears in the phase-fitting results of poloidal probe array.

Since the tearing stability is sensitive to the equilibrium current and pressure profiles, the more accurate and tightly constrained equilibrium is reconstructed using the well-measured plasma profiles using various diagnostics for the discharges in the database. The characteristics of plasma current and pressure profiles at tearing mode onset in the database of DIII-D steady-state hybrid discharges seems to be more sensitive to the global feature of plasma profile through l_i and f_p, and the effect of plasma resistivity at the mode surface through τ_R than the local feature of plasma profile through L_q and L_p. From the result of the best fit equation in the dimensionless form using r_s and τ_A, the global feature of profiles and the current profile can affect more than the local feature of profiles and the pressure profile, respectively.

The tearing stability index Δ' is calculated with the experimental equilibria in two ways, by MHD codes (PEST-III and resistive DCON) and by MRE. They are verified and validated in reasonable agreement. It is noteworthy that the determined Δ' can be positive regardless of the mode onset, so the conventional wisdom of $\Delta' > 0$ for tearing destabilization may not be the sufficient condition, rather a positive value greater than a certain threshold could replace this under the toroidal geometry.

The analytical formula of the tearing stability threshold Δ'_c is reviewed for the semi-collisional regime and the collisionless banana regime. By comparing the analytical Δ'_c with the Δ' calculated from PEST-III code near the TM onset, it is found that the condition of $\Delta' > \Delta'_c$ is required for the mode onset in the experiment. A preliminary study on the Δ'_c estimation from the normalized mode growth rate is performed by NIMROD code. The Δ'_c can be fitted for negative or marginal growth rate using the relation between the normalized mode growth rate $\gamma\tau_A$ from NIMROD and the Δ' from PEST-III.

Finally, a stability diagram of $n = 1$ tearing mode onset is suggested with local and global features of plasma profiles. Onset condition of $n = 1$ TM is analyzed by the difference between Δ' and Δ'_c, and its stability diagram is derived in terms of the local ($\nabla J_{\parallel}$ and ∇p) and global (β_N) variations for steady-state hybrid scenarios. To calculate $\Delta' - \Delta'_c$ for the stability diagram, a novel modeling package has been developed by integrating IPS/FASTRAN for equilibrium reconstruction, PEST-III/DCON for linear stability Δ' calculation, and the Δ'_c solver for analytical Δ'_c calculation. The stability boundary at the mode onset, $\Delta' = \Delta'_c$, is mapped on L_p-L_q diagram. Characteristics of this stability boundary show that the TM unstable area expands, then the stability boundary moves as β_N increases. This stability diagram can be used to design and control experiments to avoid $n = 1$ TM.

Keywords: Tearing mode onset, Tearing stability index Δ',
DIII-D Steady-state hybrid scenarios, Stability diagram

Student Number: **2011-30991**

CONTENTS

Abstract ..... **i**

Contents ..... **v**

List of Figures ..... **vii**

List of Tables ..... **xiii**

List of Abbreviations ..... **xiv**

Chapter 1. Research background and objectives **1**

1.1. Thermonuclear fusion in tokamak 2

1.2. Advanced operation scenarios for fusion reactor 7

1.3. Tearing instability in the steady-state hybrid scenarios 11

1.4. Physics of tearing mode 14

1.5. Objective and outline of this dissertation 18

Chapter 2. Experimental observations of tearing mode in DIII-D steady-state hybrid discharges **19**

2.1. Identification of the tearing mode and its onset 23

2.2. Equilibrium reconstruction with kinetic measurements constraints – Kinetic EFIT 27

2.3. Characteristics of plasma current and pressure profiles at tearing mode onset 33

Chapter 3. Determination of tearing mode stability in terms of Δ' **39**

3.1. Numerical evaluation of tearing mode stability Δ' from the MHD codes 41

3.2. Experimental estimation of tearing mode stability Δ' from the modified Rutherford equation 45

3.3. Validation and verification of determined Δ' 47

Chapter 4. Determination of the onset condition for tearing mode in terms of Δ'_c 51

4.1. Analysis of tearing instability threshold Δ'_c 53

4.2. Comparison of Δ' with Δ'_c for stable and unstable discharges of tearing mode 55

4.3. Estimation of Δ'_c from the extended MHD simulation 59

Chapter 5. Development of tearing mode onset model 65

5.1. Descriptions of tearing mode onset model 66

5.2. Construction of modeled equilibrium with the parametric variations 68

5.3. Stability boundary for tearing mode onset on L_p-L_q diagram 71

Chapter 6. Conclusions 79

6.1. Summary and concluding remarks 80

6.2. Recommendations for future work 82

Bibliography 84

Abstract in Korean 90

LIST OF FIGURES

Figure 1.1 Binding energy per nucleon vs. mass number for all naturally-occurring isotopes. Fusion-relevant isotopes are highlighted. Note logarithmic scale on the abscissa. ····· 2

Figure 1.2 Fusion cross-section of various fusion reactions against the kinetic energy of the incident particle. Note logarithmic scale on the abscissa and the ordinate. ····· 4

Figure 1.3 A schematic view of a tokamak device with currents and magnetic fields. ····· 5

Figure 1.4 Typical pressure (a) and safety factor (b) profiles of different tokamak operational scenarios. ····· 7

Figure 1.5 The current density (a) and the safety factor (b) profiles of the potential steady-state scenarios investigated on DIII-D: 'high l_i' scenario (purple), 'high q_{min}' scenario (black), 'elevated q_{min}' scenario (orange) and 'steady-state hybrid' scenario (green). ····· 9

Figure 1.6 Temporal evolution of β_N (black), amplitude of $n = 1$ (green) and $n = 2$ (red) magnitude fluctuations and q_0 (blue dashed) for discharges with different heating scenarios: (a) early NBI heating and $\beta_N^{postLH} = 2.65$, (b) no early NBI heating and $\beta_N^{postLH} = 2.65$, and (c) no early NBI heating, and $\beta_N^{postLH} = 2.6$. ····· 12

Figure 1.7 The perturbed helical flux function ψ_1, calculated using the tearing mode equation based on the current profile $j_\phi \propto (1-(r/a)^2)^3$. The discontinuity in $d\psi_1/dr$ at r_s determines stability against tearing. (a) for the (2,1) mode and (b) for the (3,1) mode. ····· 15

Figure 2.1 Time trace of typical hybrid discharge, #125469 (black) and steady-state hybrid discharge, #161170 (blue): (a) the plasma current I_p, (b) the NBI power P_{inj} and the EC power P_{EC}, (c) the normalized beta β_N, (d) the surface loop voltage V_{surf}, (e) the minimum of q profile q_{min}, (f) $n = 1$ rms amplitude and (g) $n = 2$ rms amplitude. ····· 21

Figure 2.2 Time trace of steady-state hybrid discharges with $n = 1$ tearing mode, #161172 (red) and without $n = 1$ tearing mode, #161170 (blue): (a) the plasma current I_p, (b) the NBI power P_{inj} and the EC power P_{EC}, (c) the internal inductance l_i, (d) the normalized beta β_N, (e) $n = 1$ rms amplitude and (f) $n = 2$ rms amplitude. ····· 22

Figure 2.3 Mirnov analysis overview for DIII-D experiment #161172 in the timeframe $t = 1500\,ms$ to $t = 3000\,ms$. (a) The FFT frequency spectrum, (b) $n = 1$ (yellow and red) and $n = 2$ (blue) mode amplitude, (c) the island width calculated from $(m, n) = (2,1)$ amplitude. The grey dashed line in (b) indicates the defined $(2,1)$ TM onset and the orange shade region in (b) and (c) represents the time range within $100\,ms$ for the growth rate evaluation. ····· 25

Figure 2.4 Phase-fitting results of poloidal array with toroidal mode number $n = 1$ for #161172 (a) at $t = 2450\,ms$, (b) at $t = 2460\,ms$. ··· 26

Figure 2.5 Measured and fitted profiles at the time of (2,1) TM onset for unstable discharge, #161172 (red) and at similar time for the stable discharge, #161170 (blue): (a) the electron density n_e, (b) the toroidal rotation Ω, (c) the electron temperature T_e, and (d) the ion temperature T_i. ····· 31

Figure 2.6 Profiles reconstructed by kinetic EFITs at the time of $(2,1)$ TM onset for unstable discharge, #161172 (red) and at similar time for the stable discharge, #161170 (blue): (a) the toroidal current profile $J_{\|}$, (b) the plasma pressure profile p, and (c) the safety factor q, and (d) the cross-sectional shape of the equilibria. The grey dashed line in (a)-(c) represents $q = 2$ (horizontal) and the radial location ρ at $q = 2$ (vertical). ····· 32

Figure 2.7 Time traces of representative parameters for the plasma current and pressure profiles of the steady-state hybrid discharges on DIII-D with $(2,1)$ TM onset (red). Red dashed line in the figures indicates the $(2,1)$ mode onset for each discharges. (a) the internal inductance l_i, (b) the plasma pressure peaking factor f_p, (c) the magnetic shear length L_q, and (d) the pressure gradient length L_p. ····· 34

Figure 2.8 Time traces of representative parameters for the plasma current and pressure profiles of the steady-state hybrid discharges on DIII-D without $(2,1)$ TM onset (blue). (a) the internal inductance l_i, (b) the plasma pressure peaking factor f_p, (c) the magnetic shear length L_q, and (d) the pressure gradient length L_p. ····· 35

Figure 2.9 Parameter space of the stady-state hybrid discharges on DIII-D at $(2,1)$ TM onset. (a) the internal inductance l_i, (b) the plasma pressure peaking factor f_p, (c) the magnetic shear length L_q, and (d) the pressure gradient length L_p. ····· 36

Figure 2.10 Normalized beta β_N for $(2,1)$ tearing mode onset versus the best fit to a power of l_i, $p_0/\langle p \rangle$, L_q, L_p, and τ_R. ····· 38

Figure 3.1 Schematic diagram to explain the approaches to calculate the tearing index Δ'. ····· 40

Figure 3.2 Comparison of the normalized Δ' values caldulated by PEST-III and resistive DCON ····· 47

Figure 3.3 Comparison of the normalized Δ' values caldulated by PEST-III and resistive DCON at the time of $(2,1)$ mode onset for unstable discharges (red) and for stable discharges (blue) in the database. The black circle shows the Δ' values fot other hybrid discharges to benchmark in Figure 3.2. ····· 49

Figure 3.4 Comparison of the normalized Δ' values calculated from MRE against Δ' values calculated from PEST-III at the time of $(2,1)$ mode onset for unstable discharges (red) for validation. ····· 50

Figure 4.1 Evolution of the calculated $\Delta'_c r_s$ from analytical formula by Hahm's (green) and by Shaing's (blue), and $\Delta'_c r_s$ from PEST-III (black) and from MRE (red) on time series of equilibria for unstable discharges. (a) #161172 and (b) #161169. The vertical grey dashed line indicates the defined $(2,1)$ TM onset. ····· 57

Figure 4.2 Evolution of the calculated $\Delta'_c r_s$ from analytical formula by Hahm's (green) and by Shaing's (blue), and $\Delta'_c r_s$ from PEST-III (black) on time series of equilibria for stable discharges. (a) #161170 and (b) #125469. ····· 58

Figure 4.3 The natural logarithm of the magnetic energy mode $\ln E_m$ from NIMROD for the mode growth rate. (a) the discharge with $(2,1)$ TM (#161396) and (b) the discharge without $(2,1)$ TM (#161599). ····· 61

Figure 4.4 Poincaré plots of magnetic field lines traced during a simulation with $(2,1)$ tear-type initial perturbation. ····· 62

Figure 4.5 The natural logarithm of the magnetic energy mode lnE_m from NIMROD for the mode growth rate with various plasma equilibrium and profiles with different Δ'. ····· 63

Figure 4.6 The Δ'_c estimation from the relation between the normalized mode growth rate $\gamma\tau_A$ and the Δ'. ····· 64

Figure 5.1 The overview of the procedure of the integrated modeling package for determining the tearing mode onset with current and pressure profile variations. ····· 67

Figure 5.2 The plasma profiles of modeled equilibria based on the experiment with parametric variation at the mode surface, (a) the current density profile and (b) the pressure profile. ····· 69

Figure 5.3 The plasma profiles of modeled equilibria with β_N variations, (a) the pressure profile as the reference and (b) the corresponding safety factor profile. ····· 70

Figure 5.4 The stability diagram for tearing mode on L_p-L_q parameter space using (a) the tearing stability index Δ' and (b) the critical tearing stability index Δ'_c ····· 72

Figure 5.5 The stability diagram for tearing mode on L_p-L_q parameter space using the difference between the Δ' and the Δ'_c. The black dashed line pointed out the marginal condition as $\Delta' = \Delta'_c$. The red point is the discharge with TM at onset (#161172) and the blue point is the discharge without TM (#161170). ····· 73

Figure 5.6 The stability diagram for tearing mode on L_p-L_q parameter space with various β_N, (a) $\beta_N \sim 1.5$, (b) $\beta_N \sim 2.4$, (c) $\beta_N \sim 3.0$, and (d) $\beta_N \sim 3.3$. The blue indicates stable ($\Delta' < \Delta'_c$) and the red indicates unstable ($\Delta' > \Delta'_c$) for $(2,1)$ TM stability. The black open circle indicates the experimental data at $(2,1)$ TM onset. ····· 75

Figure 5.7 The stability boundary ($\Delta' = \Delta'_c$) for tearing mode onset on L_p-L_q parameter space according to β_N, (a) $\beta_N \sim 1.5$ only (red), (b) $\beta_N \sim 2.4$ (orange), (c) $\beta_N \sim 2.7$ (green) and $\beta_N \sim 3.0$ (light blue shade), and (d) $\beta_N \sim 3.3$ (dark blue). ····· 77

LIST OF TABLES

Table 2.1 Three kinds of the equailibrium reconstrudtions according to the diagnostics and the corresponding constraints. ····· 28

Table 2.2 The global and local features of the current density and pressure profile used for the empirical estimation of the typical β_N at (2,1) mode onset. ····· 33

LIST OF ABBREVIATIONS

Here are some abbreviations commonly used in the thesis:

CER	Charge Exchange Recombination spectroscopy
DIII-D	the Doublet III with D-shaped plasma
ECE	Electron Cyclotron Emission
FFT	Fast Fourier Transform
ITB	Internal Transport Barrier
MC	Mirnov Coil array
MHD	MagnetoHydroDynamics
MRE	Modified Rutherford Equation
MSE	Motional Stark Effect
NTM	Neoclassical Tearing Mode
TM	Tearing Mode

Chapter 1.

Research background and objectives

1.1. Thermonuclear fusion in tokamak

The atoms of which every element of matter is composed have a nucleus at the center and electrons whirling about this nucleus. The nuclei of atoms are composed of protons, which have a positive electrical charge, and neutrons, which are electrically neutral. Electrons are electrically negative and have a charge equal in magnitude to that of a proton. The nucleus of an atom is held together by the strong nuclear force that binds together protons and neutrons. The interplay of attractive and repulsive forces inside atomic nuclei leads to a non-monotonic dependence of the binding energy per nucleon on the atomic number as shown in Figure 1.1. The most stable nucleus is the medium-size iron isotope ^{56}Fe.

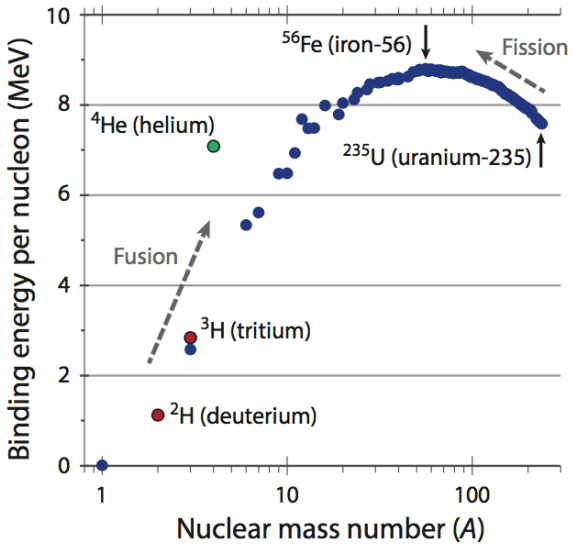

Figure 1.1 Binding energy per nucleon vs. mass number for all naturally-occurring isotopes. Fusion-relevant isotopes are highlighted. Note logarithmic scale on the abscissa.

Basically, there are two distinct exothermic processes involving the nuclei of atoms for energy production: fission, heavy atomic nucleus (like uranium and plutonium) are broken apart into lighter nuclei, and fusion, light nuclei like hydrogen are combined to form heavier nucleus such as helium. During this process, considerable amount of energy is released because the total mass of the constituents is greater than the total mass of the products. The "missing" mass, Δm, is converted into a certain amount of energy, E, given by the principle of Einstein's mass-energy equivalence, $E = \Delta mc^2$ [1].

Fusion reactions are ubiquitous throughout the universe, occurring naturally in stars such as the Sun. Unlike the proton-proton chain dominates in the Sun, there are several possible fusion reactions [2-4] that are of interest for energy production on the Earth. It is important that the large amount of energy is released per reaction and the higher peak of cross section is at lower energies as shown in the Figure 1.2.

$$^{2}_{1}D + {}^{2}_{1}D \rightarrow {}^{3}_{2}He\ (0.817\ MeV) + {}^{1}_{0}n\ (2.45\ MeV)$$

$$^{2}_{1}D + {}^{2}_{1}D \rightarrow {}^{3}_{1}T\ (1.01\ MeV) + {}^{1}_{1}H\ (3.02\ MeV)$$

$$^{2}_{1}D + {}^{3}_{1}T \rightarrow {}^{4}_{2}He\ (3.50\ MeV) + {}^{1}_{0}n\ (14.1\ MeV)$$

$$^{2}_{1}D + {}^{3}_{2}He \rightarrow {}^{4}_{2}He\ (3.67\ MeV) + {}^{1}_{1}H\ (14.7\ MeV)$$

To induce the fusion reaction, two light nuclei must come close enough together that the short-range, attractive, and strong nuclear force becomes larger than the electrostatic repulsion between their nuclei. To overcome the Coulomb barrier, the nuclei require high kinetic energies. Since fusion processes are still less probable than Coulomb scattering at each collision event, the plasma with

sufficient energy needs to be confined well enough to ensure that each particle performs many elastic collisions before it is lost. The ignition threshold to achieve the continuously stable fusion energy can be most commonly expressed in the form of the fusion triple product $nT\tau_E$. Here, n is the plasma density, T is the kinetic temperature, and τ_E is the energy confinement time.

While the gravitational force can provide the confinement with high density for fusion in case of stars, it is not appropriate in fusion reactor on the Earth because of much weaker gravitation. There are two experimental approaches to design a fusion reactor: inertial and magnetic confinement. In inertial confinement,

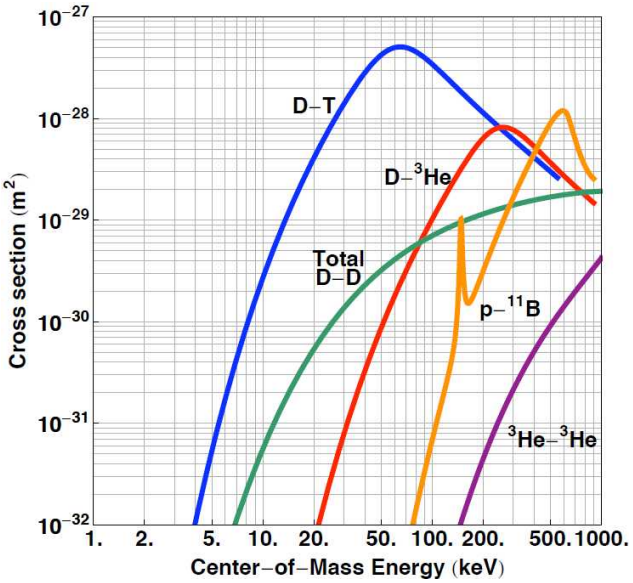

Figure 1.2 Fusion cross-section of various fusion reactions against the kinetic energy of the incident particle. Note logarithmic scale on the abscissa and the ordinate [5, 6].

a small pellet containing fusion fuel is compressed and heated by the high-powered lasers or particle beams so quickly that it reaches the conditions required for the fusion reaction. In magnetic confinement, strong magnetic fields are used to confine the hot plasma to have sufficient nuclear reactions adequate to generate the required net energy gain.

As the most successful magnetic confinement scheme to date, tokamak is a toroidal machine designed to confine a plasma in the shape of a torus (see Figure 1.3). Toroidal, poloidal and vertical magnetic fields are used to confine the plasma in a stable equilibrium. The toroidal and vertical fields are produced by magnetic

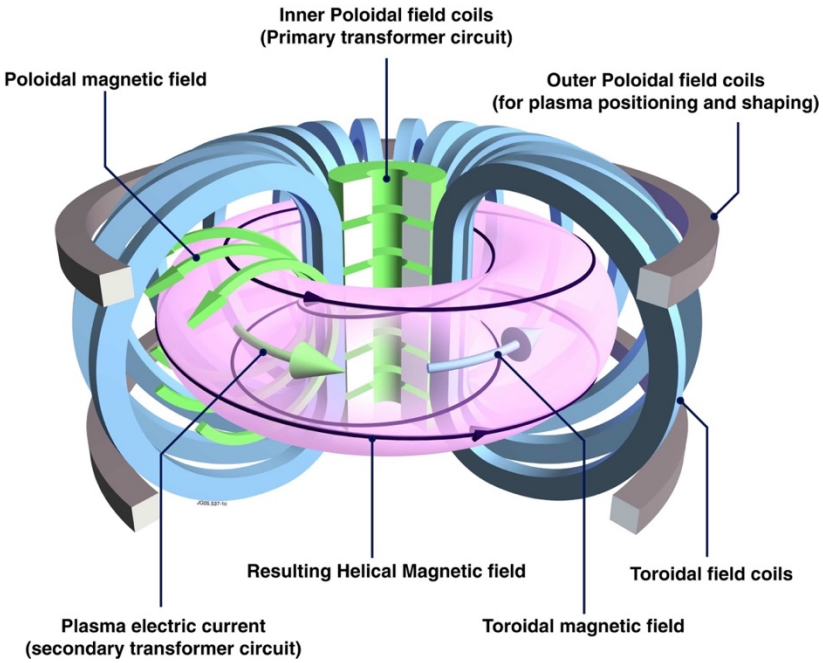

Figure 1.3 A schematic view of a tokamak device with currents and magnetic fields [7].

field coils, which are generally placed outside of the vessel, and the poloidal field is generated by the plasma current. The plasma current flows toroidally and can be generated by transformer action (inductive current drive) or by using non-inductive methods. The combination of the vertical, poloidal and toroidal fields produces a complex helical field that achieves a high level of plasma stability and longer confinement times at higher densities.

The DIII-D tokamak [8] is a medium size experimental purpose device with major radius R of $1.67\,m$, minor radius a up to $0.67\,m$, plasma current I_p up to $3.0\,MA$ and toroidal magnetic field B_T up to $2.2\,T$. The DIII-D was designed to achieve high plasma performance while maintaining the flexibility in the configuration by optimizing to allow plasma elongation κ up to 2.6 and triangularity δ up to 1.0. The actual configuration presents two divertor plates with the possibility of running discharges with one or two X points point in the upper part and/or lower part of the machine. A flexible set of heating and current drive systems are available including $20\,MW$ of neutral beam heating (NBI; co- and counter-current injection, with $5\,MW$ of variable off-axis injection and current drive), and $6\,MW$ gyrotrons with steerable launchers for EC heating, current drive, and stability control.

1.2. Advanced operation scenarios for fusion reactor

The operation scenario in tokamak researches can be globally classified by the characteristics of the shape of the radial profiles of current and pressure: conventional scenario and advanced scenario. The typical pressure and safety factor profiles in these scenarios are shown schematically in Figure 1.4.

The conventional tokamak scenarios are characterized by inductive current drive and thus the current profile has the maximum of the current density in the plasma center, resulting in a monotonically increasing q-profile. The typical scenarios are the so-called low confinement (L-mode) or high confinement mode (H-mode), of which can be distinguished by the efficiency of energy confinement.

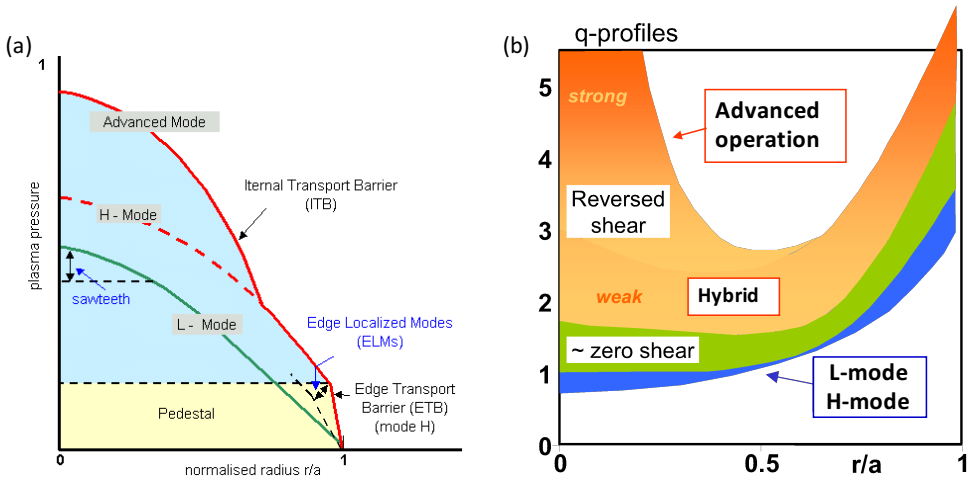

Figure 1.4 Typical pressure (a) and safety factor (b) profiles of different tokamak operational scenarios [9, 11].

The latter is characterized by a steep edge pressure gradient ('pedestal'). These operation scenarios are usually developed for pulsed operation and with a large fraction of ohmic current.

The advanced tokamak scenarios [10, 11] are characterized by non-inductive current drive with high bootstrap current fraction and the current and pressure profiles are optimized for maximum β and τ_E. These operation scenarios usually tend to have flat or even reversed, elevated q-profiles in the radial region where ∇p is significant. The current profiles are peaked off-axis and broader than conventional scenarios. The pressure profile can also exhibit a transport barrier inside the plasma, internal transport barriers (ITBs) [12, 13], by the sheared $\vec{E}\times\vec{B}$ rotation or magnetic shear for the turbulence suppression in the plasma. The hybrid scenarios are characterized by the presence of a wide central region with magnetic shear very close to zero and central q values between 1 and 1.5 [14-16]. The main advantages of this mode of operation are improved energy confinement and improved MHD stability leading to a higher β limit. These operation scenarios try to operate the fusion tokamak in steady-state.

Various advanced tokamak scenarios have been investigated on DIII-D [17-22]. These approaches can be distinguished by their respective q profiles as shown in Figure 1.5. The first approach, 'high $q_{\min}$' scenario (typically the safety factor minimum $q_{\min} > 2$) exploit broad current and pressure profiles to raise the wall-stabilized ideal MHD β_N limit and to maximize the bootstrap current fraction f_{BS}. For this scenario, very good alignment of the bootstrap current profile and the

desired plasma current profile is required, and about $10-40\,\%$ of the plasma current needs to be externally driven by either NBI or EC near the plasma periphery ($\rho\sim0.5-0.9$, where ρ is the normalized toroidal flux coordinate) to achieve steady-state operation. The second approach, 'high l_i' scenario exploit the combination of broad pressure profile and a peaked current profile to operate near the no-wall β_N limit. Since an increase in the bootstrap current J_{BS} located off-axis reduces l_i, the maintaining an elevated value of l_i as f_{BS} increases with β_N is required and the remaining of the current would be provided by external current

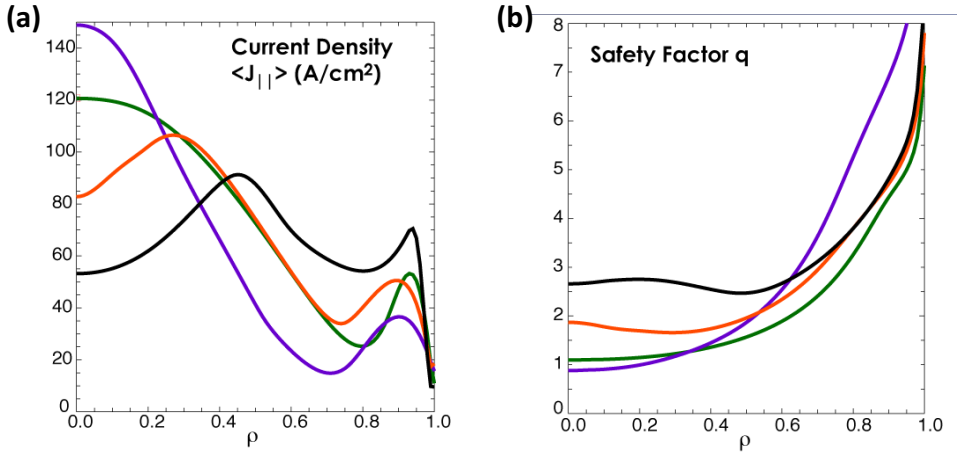

Figure 1.5 The current density (a) and the safety factor (b) profiles of the potential steady-state scenarios investigated on DIII-D: 'high l_i' scenario (purple), 'high $q_{\min}$' scenario (black), 'elevated $q_{\min}$' scenario (orange) and 'steady-state hybrid' scenario (green).

drive near the plasma center. Although the total amount of externally-driven current would be larger than in 'high $q_{\min}$' scenario, the required external current drive power could be comparable because of the high current drive efficiency at the center. The third approach, 'steady-state hybrid' scenario [23-26] exploit broad and moderate shear current profile with $q_{\min} \geq 1$. As the poloidal magnetic flux pumping out near $\rho \sim 0.35$ self-organizes the current profile due to the presence of a benign $(m, n) = (3,2)$ or $(4,3)$ modes, the external current drive can be located near the plasma center without the alignment problem as well as significant sawtooth activity. Note that the (m, n) notation describes the poloidal and the toroidal mode number, respectively.

1.3. Tearing instability in the steady-state hybrid scenarios

The tearing mode produces magnetic islands in magnetized plasmas that can significantly degrade confinement and angular momentum and even lead to plasma disruption, which is that the plasma confinement is suddenly destroyed in a high beta plasma. For example, the $(3,2)$ mode is generally found to limit performance by causing a moderate degradation in energy confinement by up to $20\ \%$ as soft-β limit, while the $(2,1)$ mode lead to an even greater loss and sometimes forms a locked mode resulting in a major disruption as hard-β limit [27].

The hybrid regime can be empirically obtained reliable access and maintained with following conditions typically in DIII-D [23]: (i) the establishment of a broad, moderate shear current profile with $q_0 > 1$ at the end of current ramp; (ii) increasing β_N sufficiently early to trigger a small $(3,2)$ tearing mode prior to the onset of sawteeth or fishbones and (iii) feedback control of β_N throughout the high performance phase. The importance of each of these is demonstrated in Figure 1.6 [23] where various waveforms from three discharges that are similar except for the early neutral beam injection (NBI) timing are compared. In the hybrid case (Figure 1.6 (a)), the subsequent increase in β_N as a result of an L-H transition and increase in NBI power and a small $(3,2)$ mode is triggered that persists for the remainder of the discharges before the onset of sawteeth. This $(3,2)$ mode acts to prevent the current profile penetration such that $q_0 > 1$ is maintained in stationary

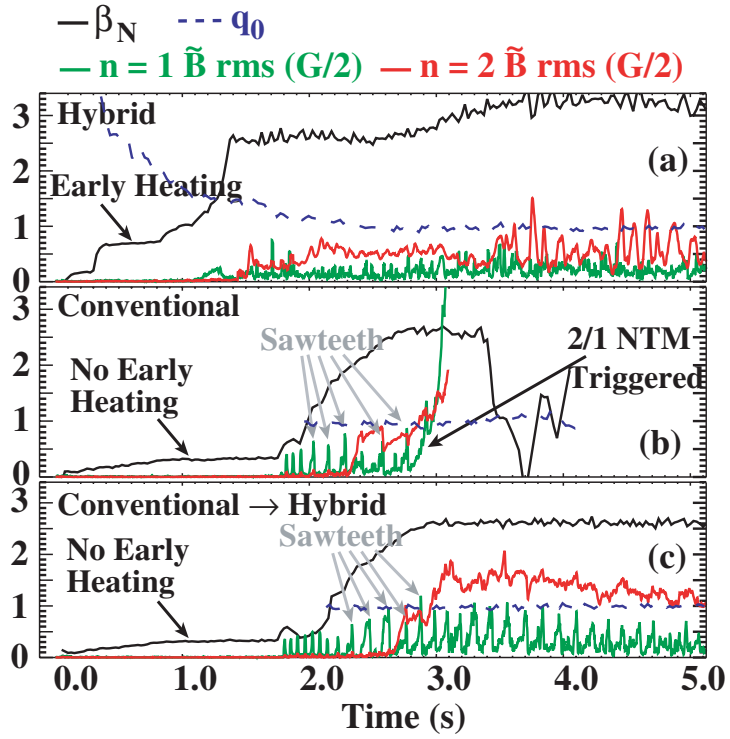

Figure 1.6 Temporal evolution of β_N (black), amplitude of $n = 1$ (green) and $n = 2$ (red) magnitude fluctuations and q_0 (blue dashed) for discharges with different heating scenarios: (a) early NBI heating and $\beta_N^{postLH} = 2.65$, (b) no early NBI heating and $\beta_N^{postLH} = 2.65$, and (c) no early NBI heating, and $\beta_N^{postLH} = 2.6$.

conditions, resulting in elimination of sawteeth (for $q_{95} > 4$) or reduction of the sawteeth amplitude to an inconsequential level (for q_{95}~4). In cases where early NBI timing is not used (Figure 1.6 (b) and (c)), sawteeth occur near the end of the current ramp. The sawteeth can trigger $(2,1)$ mode at $\beta_N = 2.65$ as shown in Figure 1.6 (b), but cannot trigger $(2,1)$ mode at $\beta_N = 2.6$ as shown in Figure 1.6 (c). It is interesting to note the sawteeth behavior after the triggering and growth of

the $(3,2)$ mode. As the $(3,2)$ mode amplitude increases, the sawteeth become smaller and the discharge begins to take on the characteristics of the hybrid discharge in Figure 1.6 (a).

The steady-state hybrid plasmas on DIII-D feature strong on-axis current drive with $q_{\min}$ slightly above 1; therefore, the anomalous broadening of the current profile by the $(3,2)$ mode is an important characteristic. While the $(3,2)$ island gives rise to a $\sim 10\,\%$ reduction in global confinement [22], this is outweighed by the benefits to stability. However, the addition of localized central ECCD can cause sawteeth to appear since the intense ECCD overwhelms the flux pumping mechanism. The $(2,1)$ TM appears more readily at high normalized pressure and, despite not causing disruptions, it degrades the confinement significantly, causing the loss of 20 to $50\,\%$ of the plasma stored energy. The tearing stability of a high β_N plasma is strongly correlated with its proximity to the ideal MHD with-wall limit [26, 28-30]. However, the physics needed to properly describe the onset threshold of the tearing mode has, until now, been unclear.

1.4. Physics of tearing mode

Classical tearing modes can grow spontaneously as the result of unfavorable current and pressure profiles. Magnetic reconnection can only occur in regions where the resistive and ideal parts of Ohm's law become comparable. There is a thin resistive layer of width δ around a rational surface, within which ideal MHD becomes invalid and resistive MHD must be used [31]. Whether the region is stable or unstable depends on global profiles and this is usually determined for a large aspect ratio tokamak by solving the cylindrical tearing mode equation for the resultant perturbed flux, $\psi(r)$.

$$\frac{d^2\psi}{dr^2} + \frac{1}{r}\frac{d\psi}{dr} - \left(\frac{m^2}{r^2} + \frac{\mu_0 \frac{dj}{dr}}{B_\theta(r)\left[1 - q(r)\frac{n}{m}\right]} \right)\psi = 0$$

Outside the resistive layer, ideal MHD can be used with appropriate boundary conditions far from the rational surface. Inside the resistive layer, resistive MHD is used. The solutions must then be matched at either side of the layer but this cannot, in general, happen without a discontinuity in the first radial derivative, $d\psi/dr$ [32]. This discontinuity is characterized by the Δ' parameter, given by:

$$\Delta' = \frac{1}{\psi}\left[\left.\frac{d\psi}{dr}\right|_{r=r_s+\delta} - \left.\frac{d\psi}{dr}\right|_{r=r_s-\delta} \right]$$

For positive Δ', the current will reinforce the initial perturbation and hence the stability of criterion for the tearing mode is unstable. Figure 1.7 [9] shows an example of the approximate analytic solution of the tearing mode equation, which assumes an equilibrium current profile of the form $j_\phi(r) \propto (1 - (r/a)^2)^3$ for the

unstable $(2,1)$ mode and for the stable $(3,1)$ mode.

It is important to note that the peak of the perturbed flux is typically inside the rational surface ($r < r_s$) for the cylindrical geometry. This means that there is a gradient in ψ either side of the rational surface and demonstrates that use of the constant-ψ approximation does not allow for a realistic island geometry. However, the constant-ψ approximation is assumed in this thesis for a simple description of the essential physics of each mechanism.

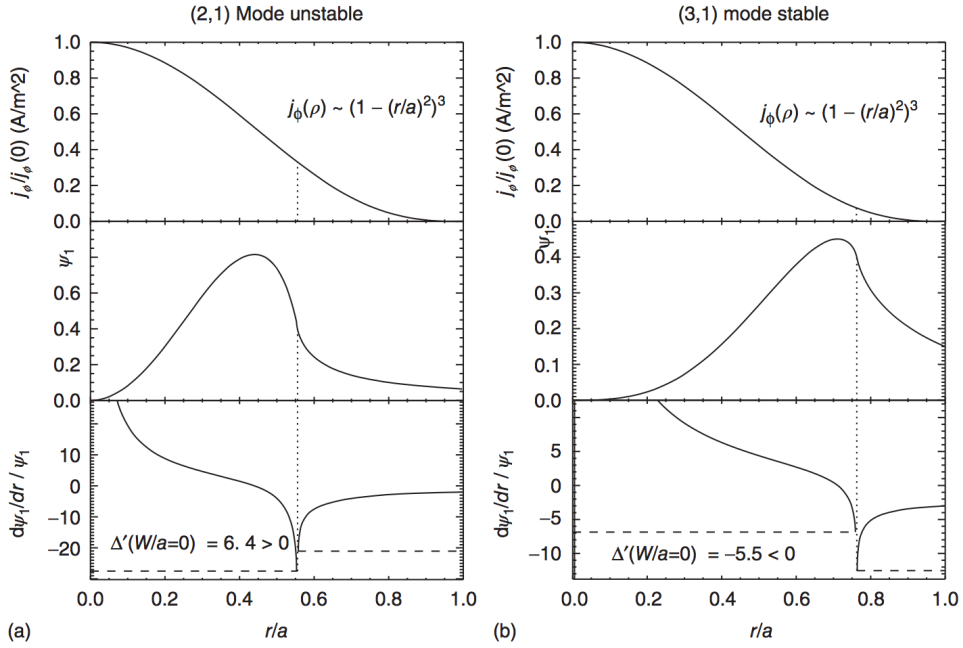

Figure 1.7 The perturbed helical flux function ψ_1, calculated using the tearing mode equation based on the current profile $j_\phi \propto (1-(r/a)^2)^3$. The discontinuity in $d\psi_1/dr$ at r_s determines stability against tearing. (a) for the $(2,1)$ mode and (b) for the $(3,1)$ mode.

According to the linear tearing mode theory with the constant-ψ assumption that the magnetic flux inside the resistive layer is constant, the mode growth rate and the resistive layer width can be obtained as $\gamma \propto \eta^{3/5}(\Delta')^{4/5}$ and $\delta \propto \eta^{2/5}(\Delta')^{1/5}$, respectively [31]. The tearing mode grows on the intermediate time scale, which is much more slowly than ideal MHD instabilities (characterized by the Alfvén time, τ_A), but much faster than the resistive diffusion of the equilibrium configuration (characterized by the resistive time τ_R). As expected, the resistive layer becomes thinner as the resistivity η decreases. Theoretically the solutions of the fields inside the resistive layer cannot be used explicitly, when δ is so small. However, the linear approximation remains valid as long as the island width stays smaller than this resistive layer width.

A highly localized jump in $d\psi/dr$ also means a spike in $d^2\psi/dr^2$, which, by Ampère's Law, gives a parallel current perturbation. This can either stabilize or destabilize a tearing mode depending on the sign of the discontinuity. The time evolution of such a mode can be evaluated by considering the resistive diffusion of the perturbed radial field in Ohm's law:

$$\frac{\partial B_r}{\partial t} = \frac{\eta}{\mu_0}\nabla^2 B_r$$

Integrating this equation across the resistive layer with the approximation of $\nabla^2 \approx d^2/dr^2$,

$$\int_{-w/2}^{+w/2} \frac{dB_r}{dt} dr \approx \frac{\eta}{\mu_0} \int_{-w/2}^{+w/2} \frac{d^2 B_r}{dr^2} dr$$

Assuming the constant ψ approximation and using B_r is independent of r,

$$w\frac{dB_r}{dt} \approx \frac{\eta}{\mu_0}\left[\frac{dB_r}{dr}\right]_{-w/2}^{+w/2}$$

Since $B_r \propto w^2$ and $B_r = m\psi/r$,

$$\frac{2\mu_0}{\eta}\frac{dw}{dt} \approx \frac{1}{\psi}\left[\frac{d\psi}{dr}\right]_{-w/2}^{+w/2}$$

Assuming the island width w is about the same as the resistive layer and using the equations for Δ', the Rutherford equation for the time evolution of the classical tearing mode width can be obtained [33],

$$1.22^{-1}\frac{\tau_R}{r_s^2}\frac{dw}{dt} = \Delta'$$

where the resistive diffusion time scale $\tau_R = \mu_0 r_s^2/\eta$ and the constant 1.22 comes from flux surface averaging in a large aspect ratio, circular cross section geometry. The island is expected to grow linearly with time if $\Delta' > 0$. However, additional effects which arises from the island region itself can also influence the island growth (recall that Δ' is a property of the global equilibrium).

1.5. Objective and outline of this dissertation

In Chapter 2, the identification of tearing mode characteristics and its onset are investigated based on the DIII-D steady-state hybrid scenario operations. The dependency of tearing mode onset on the characteristics of plasma current and pressure profiles are investigated with accurate equilibrium reconstruction with well-measured plasma profiles. In Chapter 3, the tearing stability index Δ' is calculated from the reconstructed equilibria using the MHD code and from the MRE with the experimental data. The validation and verification is presented using hybrid and steady-state hybrid discharges. In Chapter 4, the analytical formula for Δ'_c is introduced and compared with the Δ' to identify the mode onset. The critical Δ'_c tried to be estimate through the extended MHD simulation. In Chapter 5, new equilibria reconstruction with parametric variation of reference plasma profiles are performed. The dependence of mode onset stability on the profile variations was investigated. In Chapter 6, a summary and an outline of potential future work in this area are presented.

Chapter 2.

Experimental observations of tearing mode in DIII-D steady-state hybrid discharges

The experiments based on the 'hybrid' scenario has been recently performed on the DIII-D tokamak for steady-state operation by applying the electron cyclotron heating and current drive closed to the axis to achieve high efficiency. These "steady-state hybrid" experiments show the surface loop voltage decreased to zero indicating steady-state operation as well as the typical characteristics of hybrid plasma, i.e. self-organized current profile with $q_{min}\sim 1$, no sawtooth, flux pumping out near $\rho\sim 0.35$ due to the existence of dominant $(3,2)$ or $(4,3)$ modes and improved confinement than standard H-mode operation. Figure 2.1 shows a comparison of the main plasma parameters for typical hybrid discharge and steady-state hybrid discharge. Likely most hybrid plasmas, the discharges in Figure 2.1 develops a small $(3,2)$ mode during the high β_N phase, which can broaden the current profile and keep q_{min} from dropping below 1. The steady-state operation based on the hybrid regime has been demonstrated by adding central current drive from EC and NBI.

All the steady-state hybrid discharges considered in this paper have the plasma current $I_p = 1.0\ MA$, the toroidal magnetic field $|B_T| = 1.95\ T$, $q_{95}\sim 6$, and $\beta_N\sim 3-3.2$. At high β_N flattop, the $(2,1)$ TM can sometimes appear and often lock to the wall while continuing to grow. It causes the loss of β_N up to $50\ \%$ and can even cause disruptions. Figure 2.2 shows a comparison of the main plasma parameters for two different steady-state hybrid discharges, with and without the $n = 1$ mode. The slightly different timing of EC injection in Figure 2.2 (b) affected the shape of total current profile represented by l_i as shown in Figure 2.2

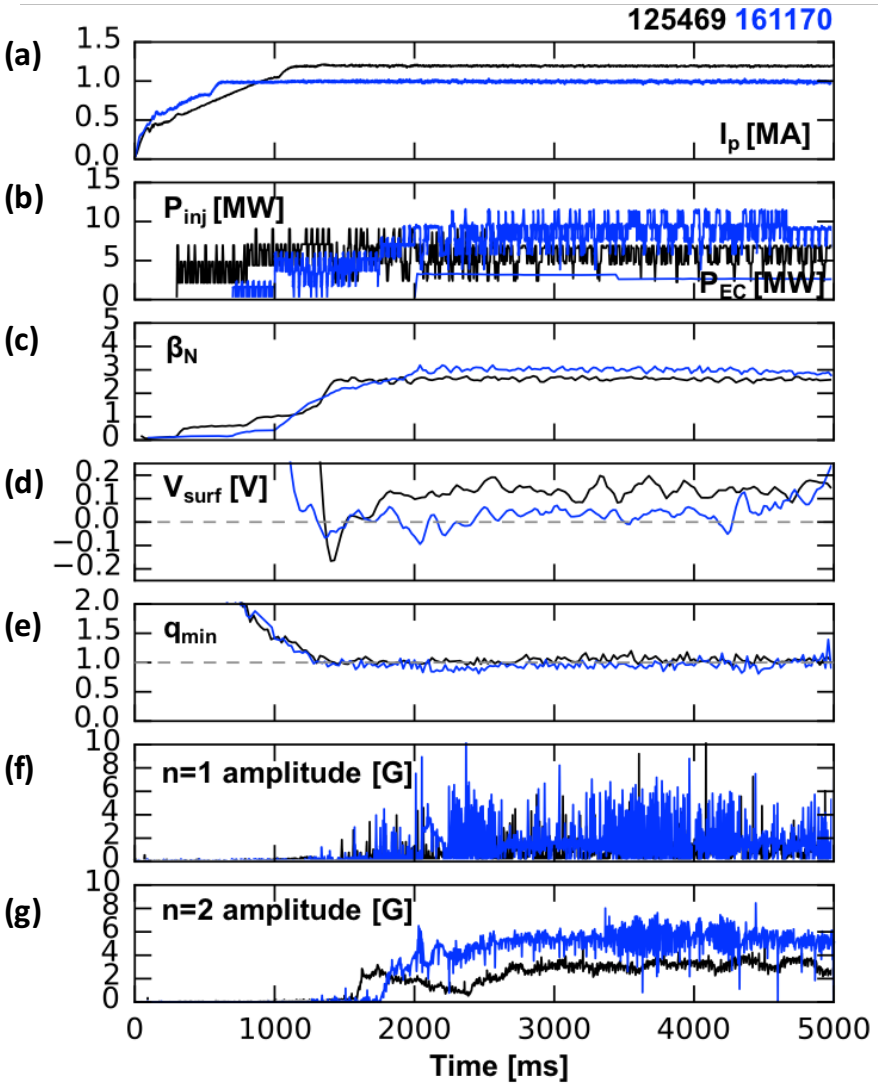

Figure 2.1 Time trace of typical hybrid discharge, #125469 (black) and steady-state hybrid discharge, #161170 (blue): (a) the plasma current I_p, (b) the NBI power P_{inj} and the EC power P_{EC}, (c) the normalized beta β_N, (d) the surface loop voltage V_{surf}, (e) the minimum of q profile $q_{\min}$, (f) $n = 1$ rms amplitude and (g) $n = 2$ rms amplitude.

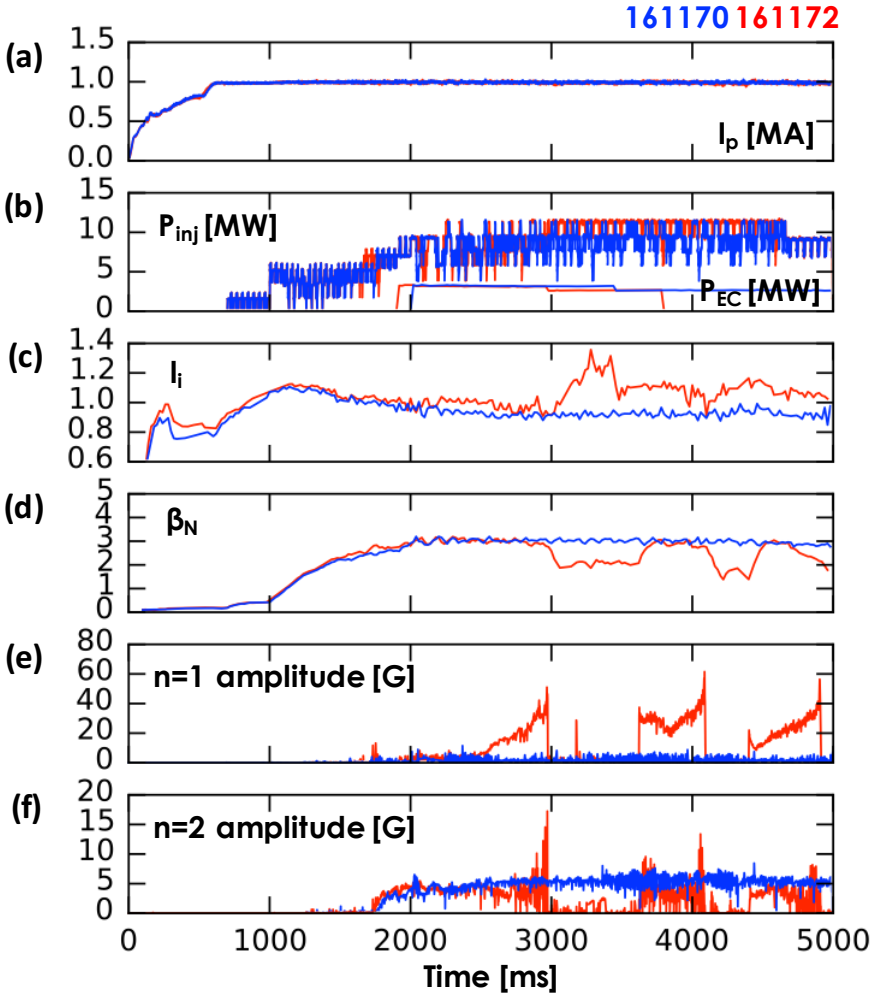

Figure 2.2 Time trace of steady-state hybrid discharges with $n = 1$ tearing mode, #161172 (red) and without $n = 1$ tearing mode, #161170 (blue): (a) the plasma current I_p, (b) the NBI power P_{inj} and the EC power P_{EC}, (c) the internal inductance l_i, (d) the normalized beta β_N, (e) $n = 1$ rms amplitude and (f) $n = 2$ rms amplitude.

(c), and then it may affect to make the $n = 1$ mode unstable.

2.1. Identification of the tearing mode and its onset

For detailed analysis of the tearing mode, the diagnostics must satisfy three basic requirements for analysis [34]:

- The measurement must be sensitive to a quantity that oscillates with the instability, i.e., the magnetic field structure, e.g., temperature, density, radiation or magnetic field component.
- The spatial distribution of observed signals from the same diagnostic must be suited for determination of the spatial mode structure.
- The sampling frequency, f_s, must be high enough.

A key ingredient for understanding the tearing mode stability is how to estimate or investigate the characteristics of the mode using available diagnostics such as magnetic probe, electron cyclotron emission (ECE) and charge exchange recombination spectroscopy (CER). The system of magnetic pick-up Mirnov probes, with acquisition frequency of $0.2\ MHz$ in DIII-D, has been mainly used to identify the mode onset, the mode amplitude and the mode number based on the fast Fourier transform (FFT) analysis [35, 36] and the phase-fitting method [37].

These magnetic probes placed on the vacuum vessel inner surface can measure the magnetic fluctuations generated by the magnetohydrodynamic (MHD) modes,

dB_θ/dt. The full radial island width [38], $w = c_{ECE}\left(16L_q R_0\left|\tilde{B}_r\right|/nB_T\right)^{1/2}$, can be evaluated from the radial helical field at the mode rational surface $\left|\tilde{B}_r\right| = 0.5\left|\tilde{B}_\theta\right|_{wall}[(R_{wall} - R_0)/r]^{m+1}$ taken from integrated perturbation amplitude $\left|\tilde{B}_\theta\right|_{wall}$ at the mode frequency filtered by Fourier and scaled to fit the island size from ECE when the island is saturated or just before locked. The mode number, (m, n) can be identified from the probe signals distributed in the poloidal and toroidal configurations and from the matching between the mode frequency and the plasma rotation frequency from CER. Figure 2.3 shows the example analysis for discharge with tearing mode onset. The $n = 1$ mode starts and begins to grow at around $2100\,ms$ in FFT spectrum of Figure 2.3 (a).

Determining that $n = 1$ mode is a TM requires careful analysis, however. Since the magnetic perturbation is detected by the probes outside the plasma, it is difficult to identify the perturbation as only a TM. Because the signal can often appear as a mixture of many modes such as ideal kink and ballooning on top of the TM, until a TM become dominant, especially with the same toroidal mode number and similar mode frequencies. The presence or absence of 'phase folding' [37, 39], reversal of $d\varphi/d\theta$ slope on the high field side during poloidal mode analysis, is used to determine the tearing mode onset because the phase folding is a typical feature of the internal kink mode due to the toroidicity and plasma shaping. In Figure 2.3 (b), there is another $n = 1$ mode before the mode onset, which is represented by yellow scatters. As shown in Figure 2.4 (a), this yellow n=1 mode

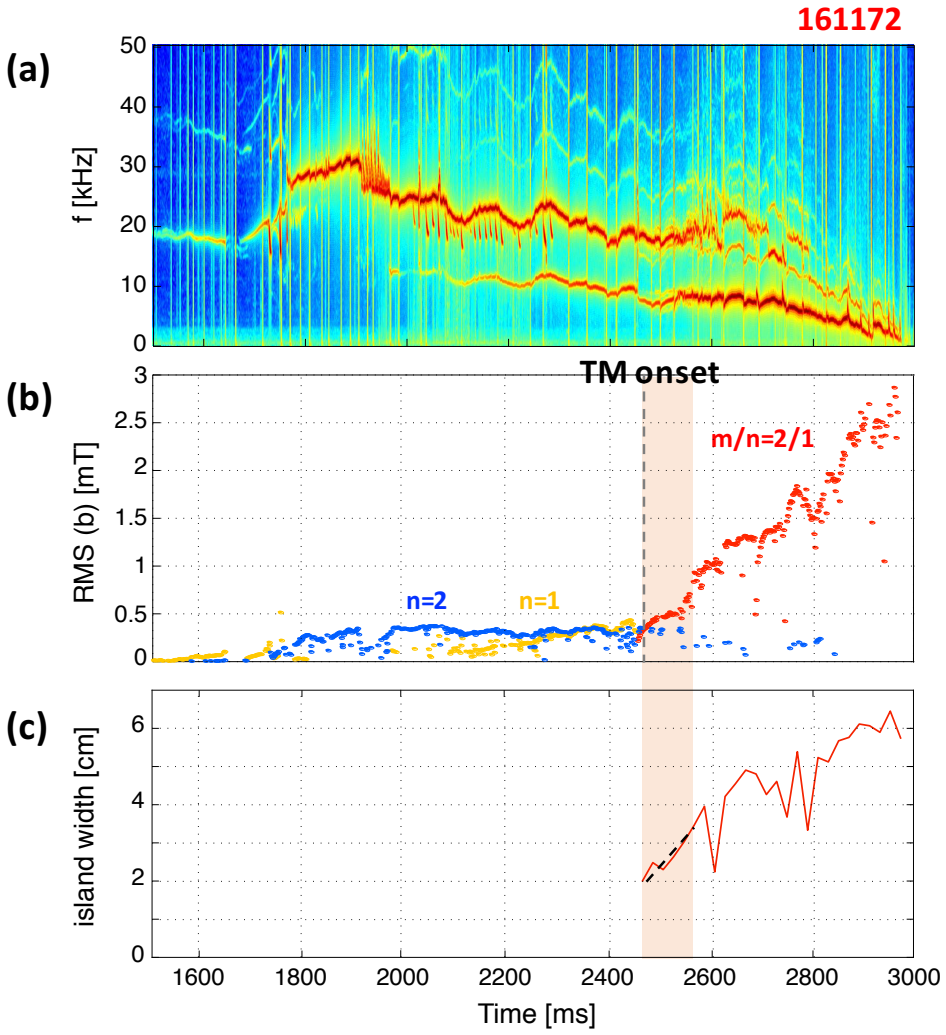

Figure 2.3 Mirnov analysis overview for DIII-D experiment #161172 in the timeframe $t = 1500\,ms$ to $t = 3000\,ms$. (a) The FFT frequency spectrum, (b) $n = 1$ (yellow and red) and $n = 2$ (blue) mode amplitude, (c) the island width calculated from $(m, n) = (2,1)$ amplitude. The grey dashed line in (b) indicates the defined $(2,1)$ TM onset and the orange shade region in (b) and (c) represents the time range within $100\,ms$ for the growth rate evaluation.

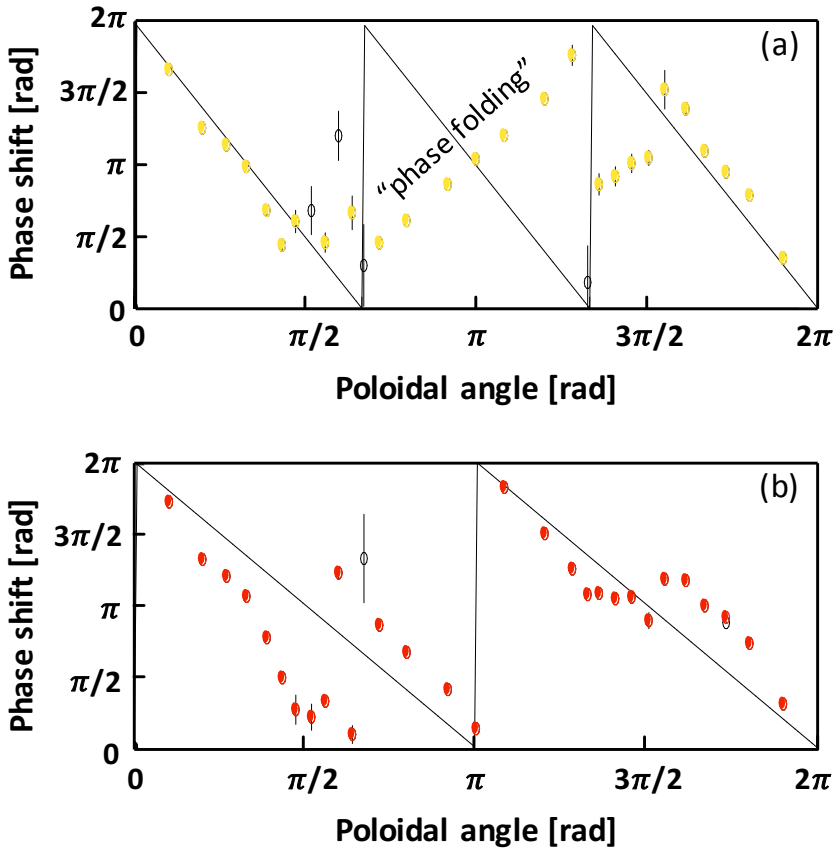

Figure 2.4 Phase-fitting results of poloidal array with toroidal mode number $n = 1$ for #161172 (a) at $t = 2450\ ms$, (b) at $t = 2460\ ms$.

makes the 'phase folding' when the mode number analysis using the Mirnov array. The 'phase folding' is disappeared slowly just after the time pointed out as "TM onset" at around $\sim 2460\ ms$ in Figure 2.3 (b).

2.2. Equilibrium reconstruction with kinetic measurements constraints – Kinetic EFIT

The equilibrium is formed by the balance of three spatially varying parameters; the magnetic flux due to the poloidal field $\psi(R,Z) \equiv -RA_\phi(R,Z)$, the toroidal filed function $f(\psi) = RB_\phi$, and the total plasma pressure $p = p(\psi)$. Here, R and Z are the radial and the vertical coordinate respectively, and A_ϕ and B_ϕ are the toroidal component of the electromagnetic vector potential and the magnetic field respectively. The equilibrium force balance equation, $\nabla p = J \times B$, can be determined as known as the Grad-Shafranov equation.

$$\Delta^* \psi = R\frac{\partial}{\partial R}\left(\frac{1}{R}\frac{\partial \psi}{\partial R}\right) + \frac{\partial^2 \psi}{\partial^2 Z} = -\mu_0 R^2 \frac{\partial p}{\partial \psi} - f\frac{\partial f}{\partial \psi}$$

The EFIT code [40, 41] solves this equation to fully reconstruct the equilibrium magnetic field, current and pressure profiles, usually assumed with two steam functions $p'(\psi) = \alpha_n y_n$ and $ff'(\psi) = \beta_n y_n$. The basis function y_n could be polynomial or tension spline functions [42] and the coefficients α_n and β_n are determined by the Picard's method to minimize the error quality function [41].

There are three kinds of the equilibrium reconstruction depending on the

diagnostics and constraints (see Table 2.1). The magnetic equilibrium reconstruction could get the plasma shape and some global plasma information such as the total plasma current $I_p = \int_\Gamma dl/R^2 B_p$, the internal inductance $l_i = \int_\Omega dV\, B_p^2/(B_{pa}^2 \Omega)$, and the poloidal beta $\beta_p = 2\mu_0 \int_\Omega dV\, p/(B_{pa}^2 \Omega)$, where Ω is

Table 2.1 Three kinds of the equailibrium reconstrudtions according to the diagnostics and the corresponding constraints.

	Diagnostics	**Constraints**
Magnetic	Magnetic loops and probes	I_p, poloidal flux, external magnetic field
Current	Motional stark effect (MSE), Soft X-ray reflectometry (SXR), etc.	Internal magnetic field or flux surface
Kinetic	Thomson scattering (TS), Electron cyclotron emission (ECE), Charge Exchange Recombination spectroscopy (CER), X-ray imaging crystal spectrometer (XCS), etc.	Pressure profile (from the measured n_e, T_e, T_i, Z_{eff}, and calculated P_f profiles), Rotation profile

the total plasma volume, Γ denotes the plasma surface bounding Ω, B_p is the poloidal component of the magnetic field, and $B_{pa} = \mu_0 I_p / \int_\Gamma dl$ is an average poloidal magnetic field for normalization. The current equilibrium reconstruction could get the current density profile $J(\psi)$ and the safety factor profile $q(\psi)$ in the plasma core using the local magnetic pitch angle B_p/B_T measured by the motional Stark effect (MSE) diagnostic. Here, ψ is the radial flux coordinate and B_T is the toroidal component of the magnetic field.

The kinetic equilibrium reconstruction with the available magnetic and kinetic measurements, as called as "kinetic EFIT" is one of the most important process for studying the MHD stabilities. It is essential to obtain detailed information on the plasma profiles, such as the current density profile $J(\psi)$, the safety factor profile $q(\psi)$ and the total pressure profile $p(\psi)$. To use the kinetic data to constrain the MHD pressure profile p in the kinetic EFIT, the measured profiles of electron density n_e, electron temperature T_e, main ion density n_i, main ion temperature T_i, impurity density n_z and pressure contributed from the fast ion p_f are required. Since these measured data are all discrete points in different spatial locations and in different temporal resolutions, they should be mapped into the flux surface coordinates using the magnetic geometry from the current equilibrium reconstruction or from the previous iteration, then fitted with smooth functions. Figure 2.5 shows the measured data and the fitted profiles at the time of (2,1) tearing mode onset for unstable discharge #161172 and at similar time stable

discharge #161170 (shown in Figure 2.2). With the hypothesis of constant temperature and density on a flux surface the total plasma pressure can be written as $p(\psi) = n_e T_e + (n_i + n_z)T_i + p_f$. The quantity n_i and n_z can be inferred from n_e by the quasi-neutrality condition and the Z_{eff} from the visible bremsstrahlung diagnostic. The pressure and density related to the fast ions are computed by the numerical code such as NUBEAM module [43] in ONETWO transport code [44]. The current profile in the edge pedestal is used as a constraint that is deduced from a time-dependent simulation of poloidal flux evolution using the ONETWO transport code.

The tearing mode stability should be analyzed with more accurate and tightly constrained equilibrium because the island that occurs at rational surface $q = m/n$ can be due to either free energy from the current profile or from the pressure profile. The reconstructed current profile, pressure profile, safety factor profile and the plasma configuration are shown in Figure 2.6. As shown in Figure 2.6 (d), these discharges have slightly different plasma shape by changing the outer squareness. The shape change might affect the peakness of the current and pressure profile as well as the pedestal property as shown in Figure 2.6. Prior to starting the detailed analysis of tearing stability, first observation shows that the local current density gradient at $q = 2$ surface for unstable discharge is greater than for stable discharge while the local pressure gradient is similar for two discharges. These observations indicate that the TM stability at the mode onset depends on the current profile, rather than on the pressure profile for this specific case.

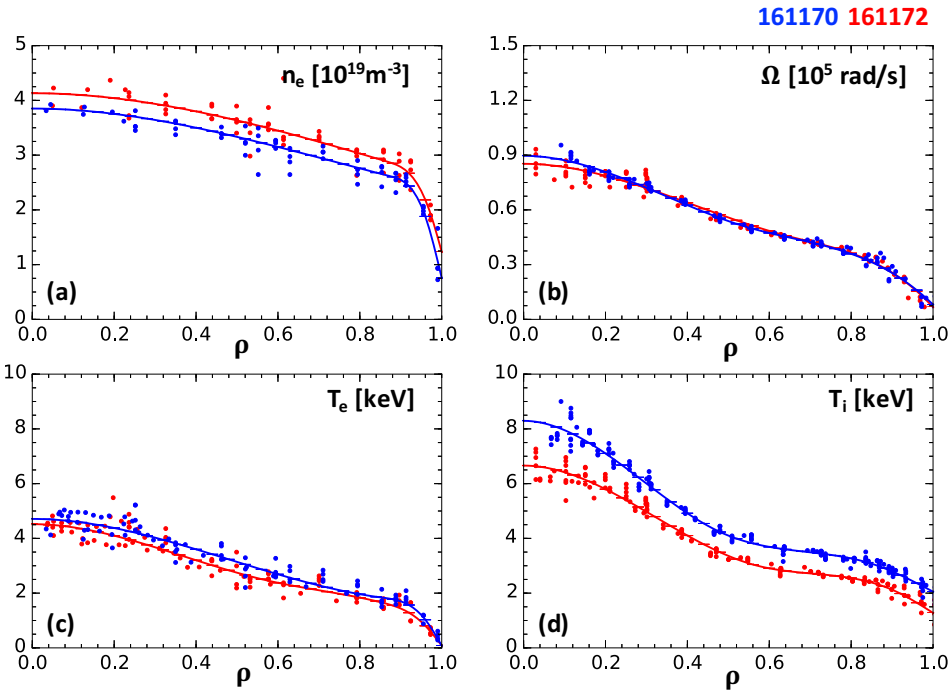

Figure 2.5 Measured and fitted profiles at the time of (2,1) TM onset for unstable discharge, #161172 (red) and at similar time for the stable discharge, #161170 (blue): (a) the electron density n_e, (b) the toroidal rotation Ω, (c) the electron temperature T_e, and (d) the ion temperature T_i.

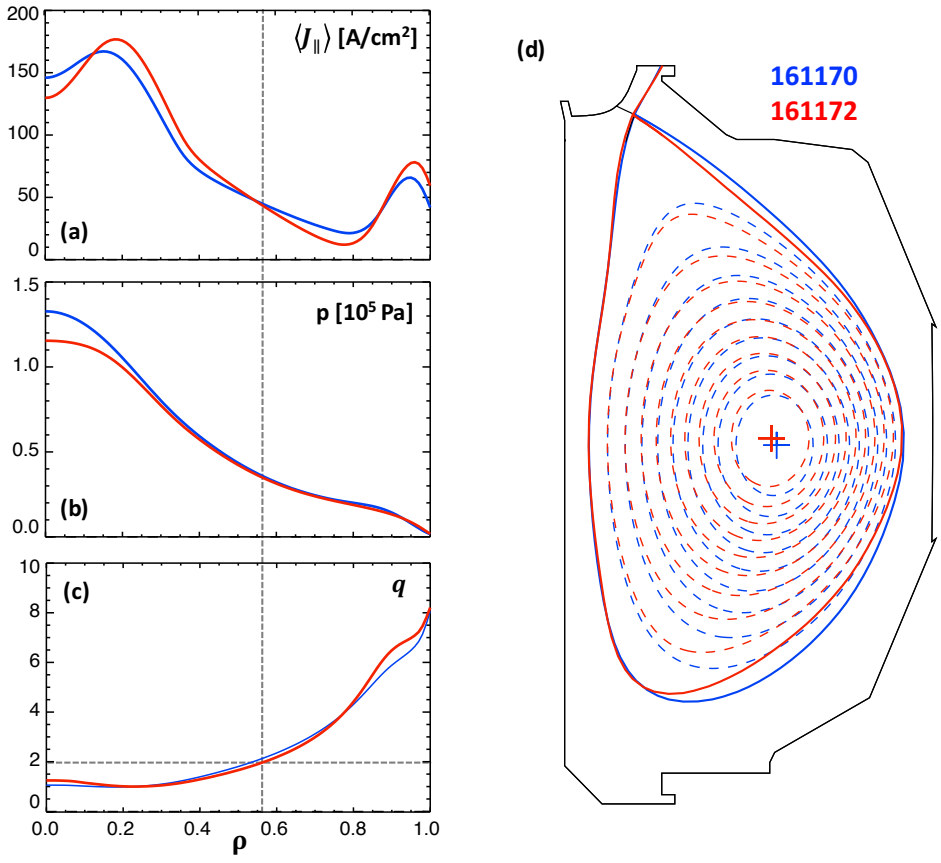

Figure 2.6 Profiles reconstructed by kinetic EFITs at the time of (2,1) TM onset for unstable discharge, #161172 (red) and at similar time for the stable discharge, #161170 (blue): (a) the toroidal current profile $\langle J_{\parallel} \rangle$, (b) the plasma pressure profile p, and (c) the safety factor q, and (d) the cross-sectional shape of the equilibria. The grey dashed line in (a)-(c) represents $q = 2$ (horizontal) and the radial location ρ at $q = 2$ (vertical).

2.3. Characteristics of plasma current and pressure profiles at tearing mode onset

With the constraints of magnetic diagnostics, the magnetic pitch angles from MSE polarimeter, pressure profile, and edge current profile, the kinetic EFIT reconstructions are performed for a database of DIII-D steady-state hybrid discharges. This database has been constructed by examining ~80 discharges, retaining only those discharges that reach plasma current 'flat top', splitting the discharge time history into $20\,ms$ slices, and retaining only those time slices which occur during the plasma current 'flat top' stage of the discharge.

To evaluate the effects of plasma equilibrium profiles at tearing mode onset, datamining of the global and local features of plasma current and pressure profiles (Table 2.2) has been conducted; the internal inductance l_i, the plasma pressure peaking factor $f_p = p_0/\langle p \rangle$, the magnetic shear length $L_q = q/(dq/dr)$, and the pressure gradient length $L_p = -p/(dp/dr)$.

Table 2.2 The global and local features of the current density and pressure profile used for the empirical estimation of the typical β_N at (2,1) mode onset.

	Global effect	**Local effect at the mode surface**
Current density profile $\boldsymbol{j(r)}$	l_i	$L_q^{-1} = \left(\frac{dq}{dr}\right)/q$
Pressure profile $\boldsymbol{p(r)}$	$f_p = \frac{p_0}{\langle p \rangle}$	$L_p^{-1} = -\left(\frac{dp}{dr}\right)/p$

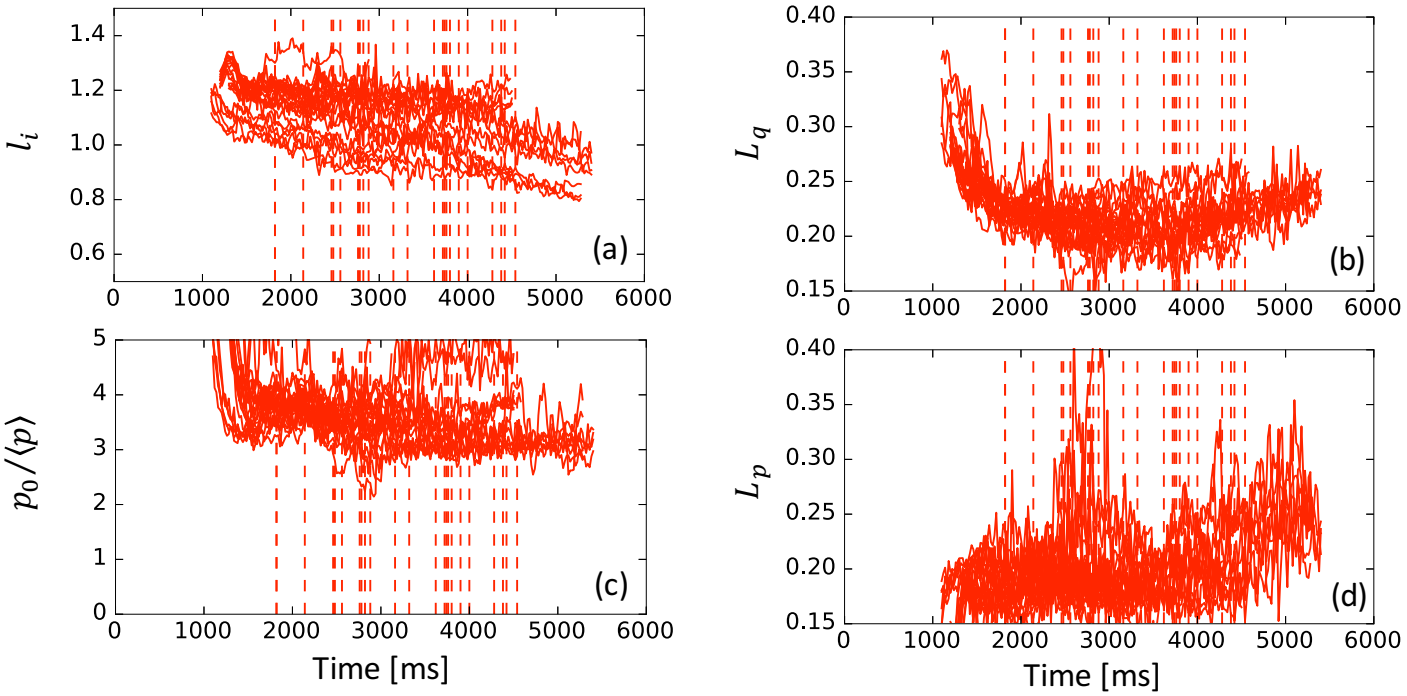

Figure 2.7 Time traces of representative parameters for the plasma current and pressure profiles of the steady-state hybrid discharges on DIII-D with (2,1) TM onset (red). Red dashed line in the figures indicates the (2,1) mode onset for each discharges. (a) the internal inductance l_i, (b) the plasma pressure peaking factor f_p, (c) the magnetic shear length L_q, and (d) the pressure gradient length L_p.

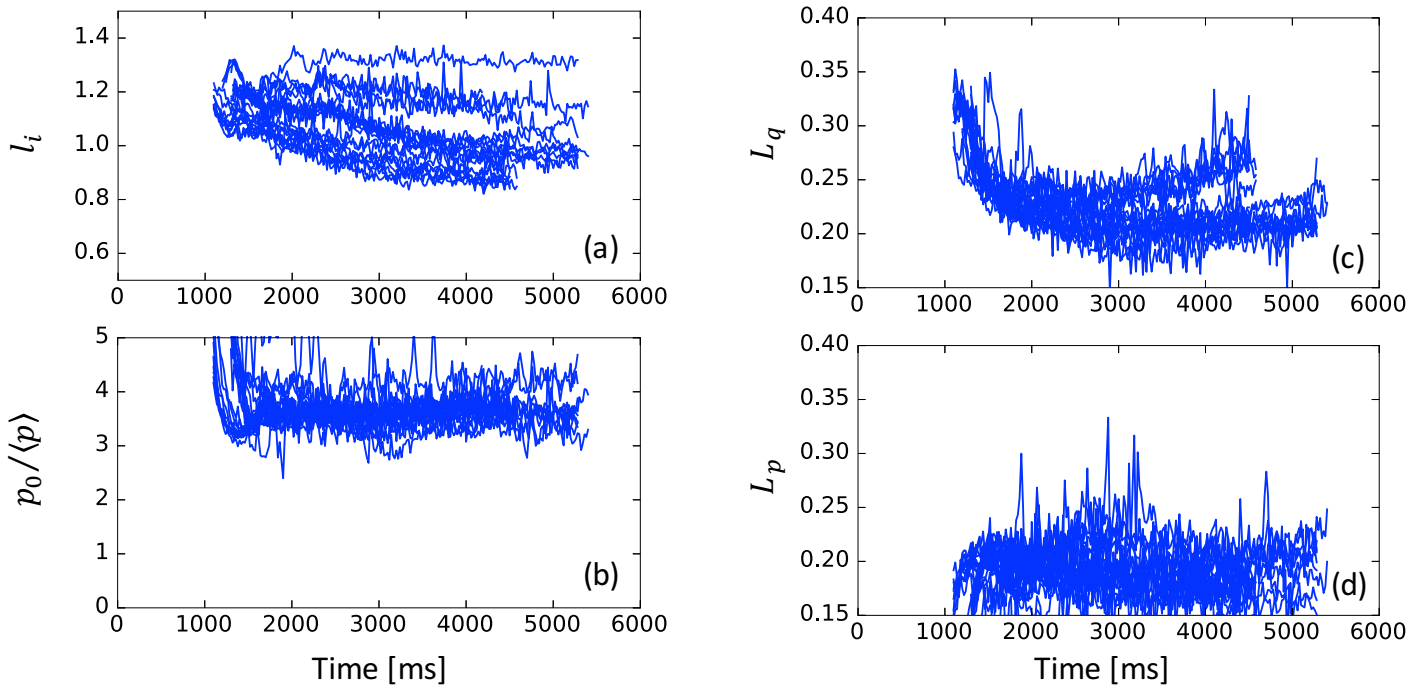

Figure 2.8 Time traces of representative parameters for the plasma current and pressure profiles of the steady-state hybrid discharges on DIII-D without (2,1) TM onset (blue). (a) the internal inductance l_i, (b) the plasma pressure peaking factor f_p, (c) the magnetic shear length L_q, and (d) the pressure gradient length L_p.

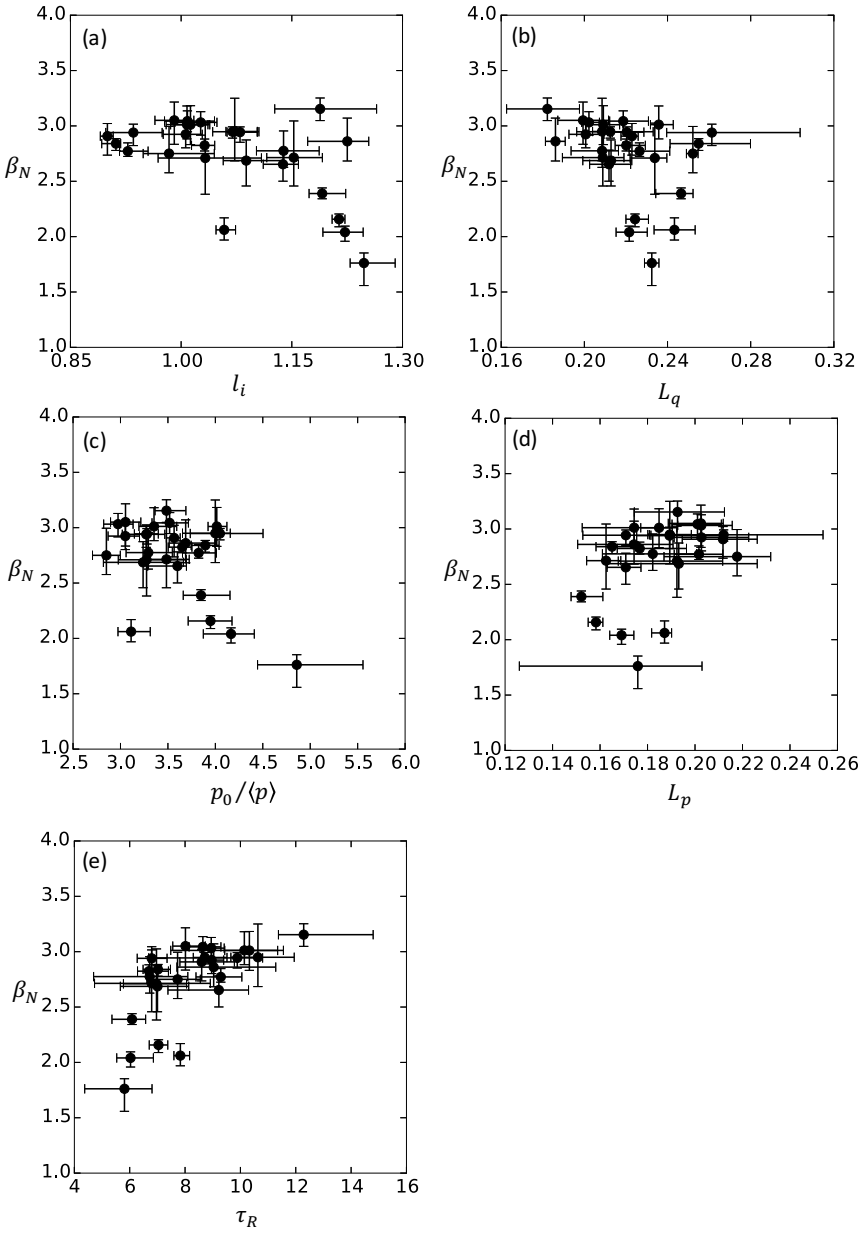

Figure 2.9 Parameter space of the stady-state hybrid discharges on DIII-D at (2,1) TM onset. (a) the internal inductance l_i, (b) the magnetic shear length L_q, (c) the plasma pressure peaking factor f_p, (d) the pressure gradient length L_p and (e) the local resistive diffusion time τ_R.

Figure 2.7 and Figure 2.8 shows the time traces of these representative parameters for the plasma current and pressure profiles of the steady-state hybrid discharges on DIII-D with and without (2,1) TM onset, respectively. The difference of parameter ranges between stable and unstable discharges cannot be distinguished clearly, and each parameter is within a certain broad operation range.

The normalized β_N at (2,1) TM onset in steady-state hybrid experiments are represented by a best fit in terms of five plasma parameters related with the characteristics of plasma current and pressure profiles (shown in Table 2.2) and the effect of plasma resistivity at the mode surface as $\tau_R = \mu_0 r_s^2/\eta$. Here, r_s is the minor radius of the mode surface. The figures of β_N against each parameter at (2,1) TM onset are shown in Figure 2.9. The (2,1) TM onset seems to be more sensitive to the global feature of plasma profile through l_i and f_p than the local feature of plasma profile through L_q and L_p. However, the local feature of plasma profile cannot be ignored when the change ratio of the parameter space was considered. The trend of best fit equation shows that (2,1) tearing mode stability is correlated with these parameters.

$$\beta_N(FIT) = 0.41 l_i^{-1.08} f_p^{-0.26} \left(L_q^{-1}\right)^{0.81} \left(L_p^{-1}\right)^{0.36} \tau_R^{0.21}$$

This best fit equation can be written in the dimensionless form using r_s and τ_A,

$$\beta_N(FIT) = 0.05 l_i^{-1.14} f_p^{-0.31} \left(r_s L_q^{-1}\right)^{0.49} \left(r_s L_p^{-1}\right)^{0.18} (\tau_R/\tau_A)^{0.25}$$

This empirical scaling based on the database shown in Figure 2.10, indicates that broad global current profile, strong magnetic shear at the mode surface, strong pressure gradient at the mode surface, broad global pressure profile, and long resistive diffusion time at the mode surface are good to achieve high β_N without (2,1) TM.

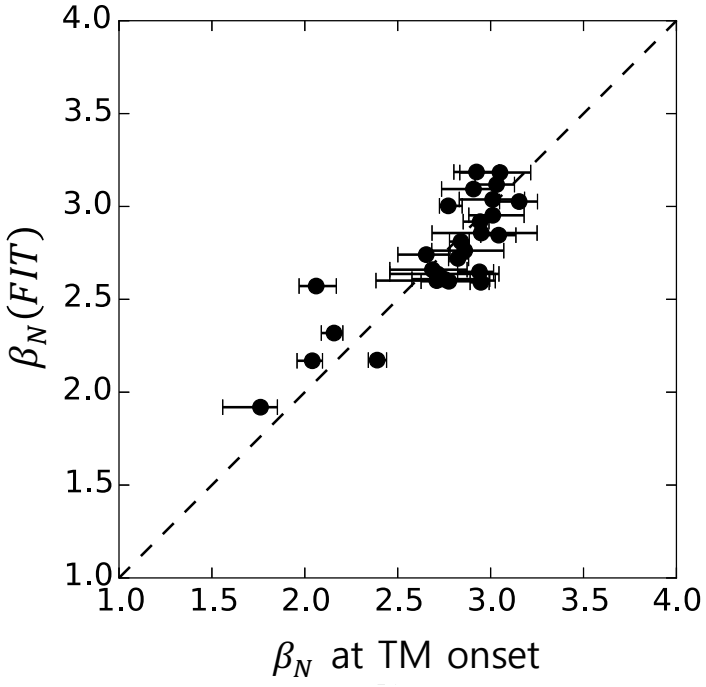

Figure 2.10 Normalized beta β_N for (2,1) tearing mode onset versus the best fit to a power of l_i, $p_0/\langle p\rangle$, L_q, L_p, and τ_R.

Chapter 3.

Determination of tearing mode stability in terms of Δ'

Tearing stability is determined by the classical tearing index Δ', which defined by the difference of ψ gradient at mode surface. The change in the plasma magnetic energy due to the TM is $\delta W_{mag} \propto -\Delta'$ [45]. Thus, the TM is linearly unstable as there is free energy available for reconnection when $\Delta' > 0$. The computation of Δ' can be made from the MHD equilibrium provided it is accurately measured or reconstructed.

In this chapter, the Δ' can be obtained by two approaches; global and local approach. The first one is performed by MHD code using the outer solution from

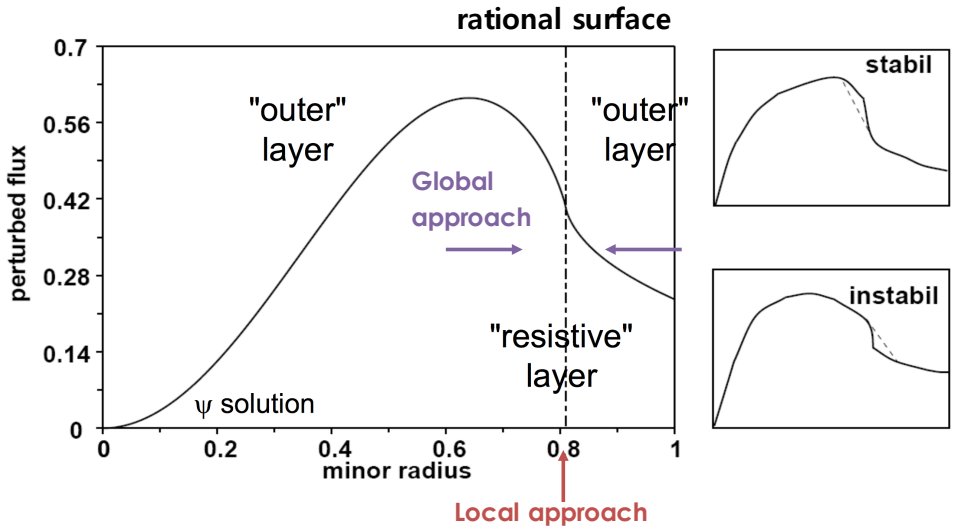

Figure 3.1 Schematic diagram to explain the approaches to calculate the tearing index Δ'.

the Δ' definition. The second one is inferred from the modified Rutherford equation using the local characteristics at the rational surface measured by diagnostics.

3.1. Numerical evaluation of tearing mode stability Δ' from the MHD codes

A resistive stability code, PEST-III [46, 47] can calculate the Δ' from the ratio of the lowest order in the Frobenius expansion coefficients of the small and large solution of the MHD stability equation for finite pressure with an arbitrary geometry. It is used to analyze a time series of experimental equilibria in this thesis.

To study linear resistive MHD in the asymptotic matching approach by PEST-III, the problem separates naturally into three parts: the inner layer within resistive layer, the outer region considered as ideal MHD, and a matching problem between them. For the outer region in cylindrical geometry, $L\xi = \frac{\partial}{\partial\psi} f \frac{\partial\xi}{\partial\psi} - g\xi = 0$ where ξ is the displacement, ψ is the normalized poloidal flux variable and f and g are scalar functions of the equilibrium profiles, while in toroidal geometry, L is the analogous second-order operator [46, 48]. This equation has two independent solutions; a regular solution and a singular solution at resonant surfaces. The "non-resonant" or "small" solution associated with ideal MHD instability and the "resonant" or "large" solution associated with resistive instability are obtained by the Frobenius expansion of the regular solution and a singular solution,

respectively. The combination of these two solutions across rational surfaces gives rise to two related types of singular modes, i.e., tearing (or reconnecting) and interchange modes, distinguished by a local variation with either an odd or even parity across the rational surface, respectively. In general, in a torus some mixture of the two parities exists at a given rational surface.

For a given toroidal eigenvalue n, the $2N\times2N$ matrix relating the singular coefficients of the two parities that describe the ideal MHD outer region solution for a torus with N resonant surfaces $q = m/n$ in the plasma: $m = 1,2,\dots,N$.

$$D' \equiv \frac{1}{2}\begin{bmatrix} \Gamma' & B' \\ A' & \Delta' \end{bmatrix}$$

Here, Δ' couples the two negative parity "tearing" components, Γ' the two positive parity "interchange" components, and A' and B' the negative to positive and positive to negative parities, respectively. The resistive mode growth rate can be determined by matching the outer region matrix to an independently determined matrix describing the corresponding coefficients of the inner layer solution at each $q = m/n$ to determine the growth rates of instabilities at the different surfaces. The stability is then determined by solving the matching condition,

$$\det[D' - D(Q)] = 0$$

where $D(Q)$ is the solution vector inside of the resonant layer and Q is the normalized growth rate.

As another approach, the DCON code [49] for the ideal MHD stability has been recently extended to compute the outer region solution based on the precise

asymptotic matching method including full mode coupling and multiple singular surfaces. The robust solution for resistive instability as well as Δ' can be obtained with more reliable convergence by improving a Galerkin method using advanced basis function and the flexible packing algorithm.

There is a Hilbert space of finite ideal MHD energy solutions, $\delta W < \infty$. In each singular surface, there are large and small resonant solutions for $m = nq$, as well as nonresonant solutions for the Fourier components $m \neq nq$. The large resonant solutions are not elements of the Hilbert space, but they drive finite-energy responses. Treating the large solutions as inhomogeneities, we compute the response in the Hilbert space by solving an inhomogeneous linear equation, the Euler-Lagrange equation for minimizing δW, which is also the equation of motion for zero-frequency modes. The Euler-Lagrange equation has the form

$$L\Xi \equiv (F\Xi + K\Xi)' - (K^{\dagger}\Xi' + G\Xi) = 0$$

where ψ is a flux coordinate; $\Xi(\psi)$ is a complex M column vector of Fourier coefficients of the normal plasma displacement; and the Hermitian matrices F and G and the non- Hermitian matrix K are $M \times M$ complex matrices derived from equilibrium quantities. The inhomogeneous equation is $L\Xi_{Hilbert} = -L\Xi_{large}$ with matrix form by expanding Ξ in a set of Galerkin basis functions. The choice of basis functions determines the rate of convergence. To improve the radial basis functions, C^1 Hermite cubics to resolve the nonresonant solutions and Frobenius power series to resolve the large and small resonant solutions were used on a more flexible packed grid in ψ. The best convergence of the poloidal Fourier series in a

variety of straight-fieldline coordinates is obtained with Hamada coordinates. Equilibrium quantities are fit to bicubic splines in ψ and θ, which allows us to compute convergent Frobenius expansions to arbitrarily high order.

The matching matrix Δ' is constructed from the coefficients of the small resonant solutions driven by the large resonant solutions. For N singular surfaces, there are $2N$ large solutions, on the left and right of each singular surface, each of which drives $2N$ small solutions, making Δ' a $2N \times 2N$ matrix. The ideal and outer region solutions are completely determined by DCON, leaving only the coupling matrix for the inner region, which can be considered independently by MATCH module.

These codes were calculated with the same inverse equilibria refined by the TEQ inverse equilibrium solver [50] in the CORSICA code [51] to get the higher grid resolution and to check the ideal MHD stability. A conformal conducting wall was considered for the DIII-D vacuum vessel located at 1.4 times minor radius. In this thesis, Δ' calculations for $(2,1)$ mode was only considered but the other modes at $q = 3$, 4, and 5 with $n = 1$ were also included to determine the matching matrix from the outer ideal MHD solutions. It is noteworthy that the equilibria must be ideal MHD stable and the rational surface should not be located at the very near magnetic axis, separatrix, or extremum of safety factor to perform a valid calculation of Δ'.

3.2. Experimental estimation of tearing mode stability Δ' from the modified Rutherford equation

In addition to the Ohmic current, there are a number of currents which contribute to the perturbed parallel current ($J_{\parallel}$) on tokamaks, influencing island stability and growth. These include the bootstrap current (J_{bs}), the ion polarization current by inertia effects such as the diamagnetic drift, the finite perpendicular transport, the finite Larmor radius, etc., the equilibrium pressure gradient and the favorable curvature in a toroidal geometry (J_{pol}), and the EC driven current (J_{EC}). If the effects of these currents are included in the classical Rutherford equation, we obtain the modified Rutherford equation (MRE) which more accurately describes the evolution of an island more accurately:

$$\frac{\tau_R}{r_r^2}\frac{dw}{dt} = \Delta'_0 + \Delta'_{bS} + \Delta'_{pol} + \Delta'_{EC}$$

The MRE encapsulates the stability of neoclassical tearing mode (NTM) although the governing physics of the equation is not yet conclusive. According to physical assumptions adopted in the analysis and the target plasma condition, the detailed representation of the terms in the MRE can be different although it represents the same effect.

For the plasmas considered in this thesis, the Δ'_{EC} term can be ignored because no electron cyclotron current drive (ECCD) is used to directly suppress the $(2,1)$ TM or the $(3,2)$ TM. The MRE for tearing stability and the evolution of an island width w [52] employed in this thesis is given by

$$1.22^{-1}\frac{\tau_R}{r_s}\frac{dw}{dt} = \Delta' r_s + \varepsilon^{1/2}\frac{r_s L_q}{L_{pe}}\beta_{\theta e}\left[\frac{1}{w} - \frac{w_{marg}^2}{3w^3}\right]$$

where r_s is the minor radius of the mode and $\tau_R = \mu_0 \sigma \kappa r_s^2 T_e^{3/2}/Z$ is the local resistive diffusion time from Spitzer resistivity. Here, κ is the elongation of the resonant surface, Z is the effective charge number, and σ is the Spitzer factor. $\varepsilon = r_s/R$ is the inverse aspect ratio for the major radius R, $L_q = q/(dq/dr)$ and $L_{pe} = -p_e/(dp_e/dr)$ are the magnetic shear length and the electron pressure gradient length, respectively, and $\beta_{\theta e} = 2\mu_0 k_B n_e T_e/B_\theta^2$ is the electron poloidal beta. The effective marginal island width $w_{marg} \approx 2\varepsilon^{1/2}\rho_{\theta i}$ is typically assumed about twice of the trapped ion banana width, $\varepsilon^{1/2}\rho_{\theta i}$, with the ion poloidal Larmor radius $\rho_{\theta i} = (2m_i T_i/eB_\theta^2)^{1/2}$.

The classical tearing index Δ', defined as the discontinuity at the rational surface in the logarithmic derivative of the perturbed magnetic potential [33] as described in the previous chapter, can be inferred experimentally from the MRE using kinetic EFIT and the measured plasma profiles at onset. However, it can be applied only for discharges with TM because the island width and its growth rate are required. Since the TM can initially grows exponentially in time when the island is small and then grow linearly in time [53], the growth rate can be evaluated by the linear fit to the calculated island width within $100\,ms$ from the mode onset defined in section 2.1, generally linear fit because of the larger initial island size.

3.3. Validation and verification of determined Δ'

A comparison of the tearing stability index Δ' from the outer region between PEST-III and resistive DCON for the (2,1) rational surface in hybrid discharges is performed to benchmark as shown in Figure 3.2. Here, the set of equilibria are reconstructed regardless the TM existence. These codes have different coordinate system to calculate the Δ', but the calculated Δ' show a good agreement as shown in Figure 3.2.

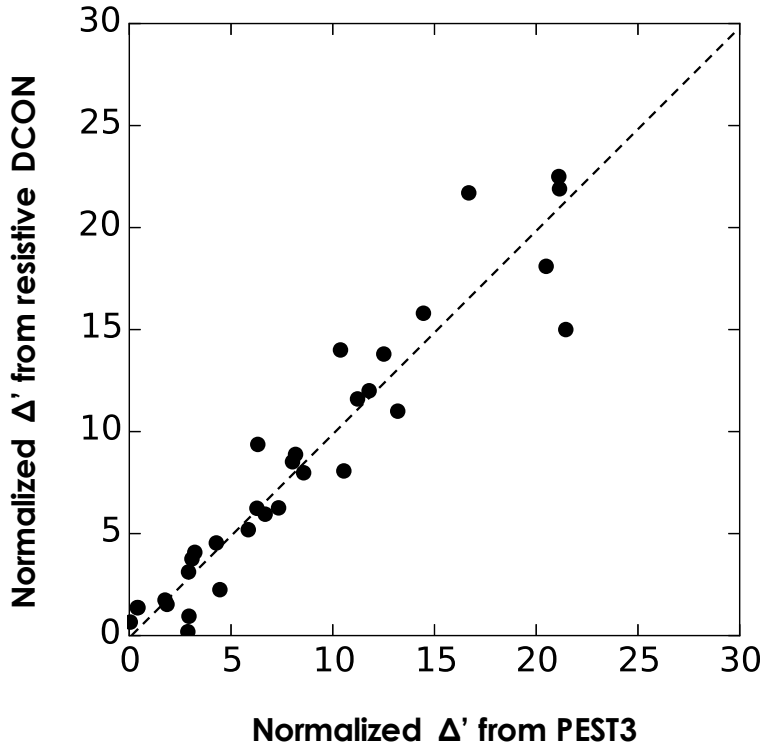

Figure 3.2 Comparison of the normalized Δ' values caldulated by PEST-III and resistive DCON.

Unstable discharges for (2,1) TM during the β_N flattop in the analyzed database were used to calculate the normalized Δ' from the stability codes, PEST-III and resistive DCON and the Δ' values from MRE. Figure 3.3 and Figure 3.4 shows the comparison where a reasonable qualitative agreement is observed between the Δ' values. The red points refer to the Δ' calculated with the equilibrium at (2,1) mode onset while the blue ones without TM in Figure 3.3. If there's no available equilibrium at the precise point at mode onset, the equilibrium close to the mode onset is used. Note that the stability codes can calculate Δ' in any discharges, but the discharges with (2,1) TM onset were only selected for comparison with MRE.

It is worth to give a few remarks as follows: First, the determined Δ' in the Figure 3.3 can be positive regardless of the mode onset, but Δ' for stable discharges are relatively smaller. It would suggest that the conventional wisdom of $\Delta' > 0$ for tearing destabilization may not be the sufficient condition, rather a positive value greater than a certain threshold could replace this under the toroidal geometry. Second, the PEST-III results show lower Δ' than the MRE results for some cases in Figure 3.4. It is possible due to the overestimation of the island growth rate in MRE calculations or the uncertainty of equilibrium at the mode onset in PEST-III calculations.

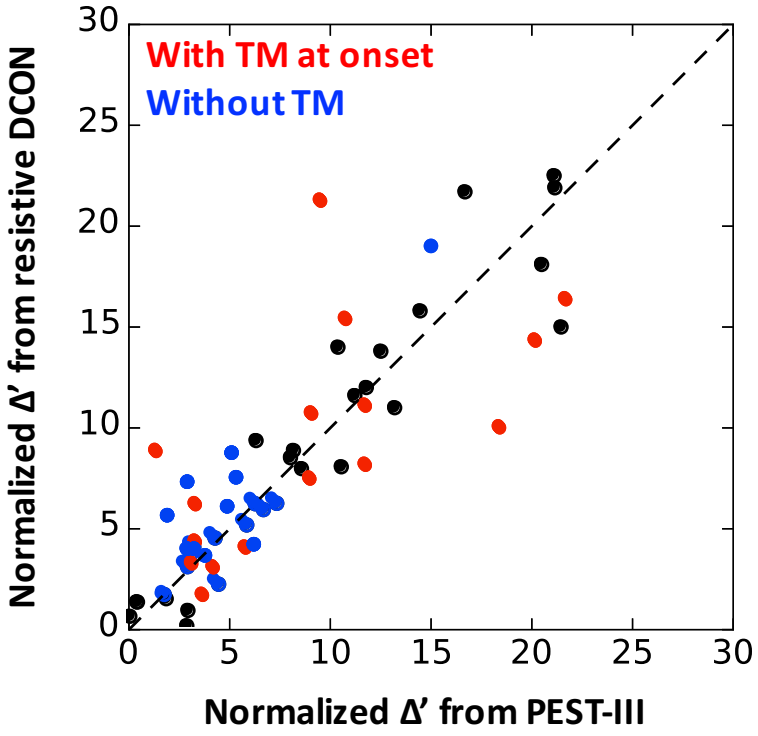

Figure 3.3 Comparison of the normalized Δ' values caldulated by PEST-III and resistive DCON at the time of $(2,1)$ mode onset for unstable discharges (red) and for stable discharges (blue) in the database. The black circle shows the Δ' values fot other hybrid discharges to benchmark in Figure 3.2.

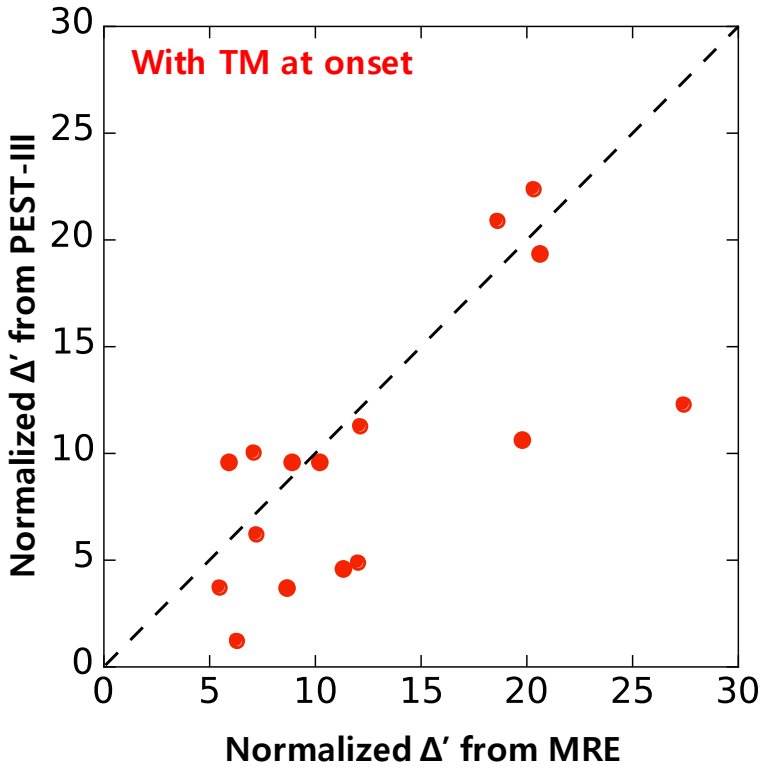

Figure 3.4 Comparison of the normalized Δ' values calculated from MRE against Δ' values calculated from PEST-III at the time of (2,1) mode onset for unstable discharges (red) for validation.

Chapter 4.

Determination of the onset condition for tearing mode in terms of Δ_c'

In the pioneering work based on the resistive MHD description [32], it has been shown that tearing instabilities occur when the classical tearing index Δ' is positive. This usual tearing instability criterion $\Delta' > 0$ can be modified to $\Delta' > \Delta'_c > 0$, where $\Delta'_c \propto \eta_{\parallel}^{-1/3} |D_R|^{5/6}$ [54], $\eta_{\parallel}$ is the parallel resistivity and D_R is the resistive interchange driving term as a results of good average curvature in a toroidal plasma. There have been various follow-up studies of this tearing stability threshold Δ'_c analytically.

In this chapter, the analytical tearing stability threshold Δ'_c in the semi-collisional regime [55] and the collisionless banana regime [56] is reviewed, including their basic descriptions and the properties for a range of plasma parameters. These analytical Δ'_c will be calculated with the experimental equilibrium and profiles to evaluate the tearing stability by comparing with the Δ' calculated from PEST-III code near the TM onset. As the numerical approach to obtain Δ'_c, the mode growth rate calculated by the extended MHD code is fitted with the calculated Δ'.

4.1. Analysis of tearing instability threshold Δ_c'

In high-temperature tokamak plasmas, additional kinetic and geometrical effect on the tearing stability become very important such as the finite ion gyroradius effects and the effects associated with the parallel gradient of the electron pressure. The effects associated with the predominantly electrostatic perpendicular electric field lead to a significant reduction of the mode growth rate. When the tearing mode growth rate calculated from the resistive MHD is smaller than the electron diamagnetic frequency, the mode becomes a so-called drift-tearing mode with real frequency near $\omega_{*e} = T_e k_y / eBL_n$, where $L_n = -[(d/dr)\ln n_0]^{-1}$ is the density gradient scale length and k_y is the poloidal wavenumber. In the drift-tearing regime, with resistivity as the only dissipative effect, the unstable mode structure ceases to be spatially localized. Further, when the resistivity becomes so small that the effective ion-Larmor radius at the electron temperature, $\rho_s = \sqrt{T_e/M_i}(M_i/eB)$, is greater than the resistive layer width, the mode becomes the so-called semicollisional tearing mode. Similarly to the electron diamagnetic frequency effects, the semicollisional effects are introduced by the electron density gradient in the generalized Ohm's law.

Analysis of the dispersion relation shows that semicollisional drift-tearing modes can be stabilized by plasma compression and good average curvature [54]. The instability threshold in terms of physical parameters when $L_n/L_s > \beta/|D_R|$ is given by [55]

$$r_s\Delta_c' \cong 0.35(-D_R\beta)^{1/2}(r_s/\rho_s)$$

as the results of the good average curvature effects when the perpendicular resistivity is large. Meanwhile, the instability threshold with the opposite limit $L_n/L_s < \beta/|D_R|$ is given by

$$r_s\Delta_c' \cong 0.37\beta(r_s/\rho_s)(L_s/L_n)^{1/2}(1+2q^2)^{1/4}$$

as the results of the plasma compression effects including ion sound waves when the perpendicular resistivity is negligible. It is interesting to note that Δ_c' is independent of the resistivity in both cases.

In the collisionless banana regime, the primary destabilization mechanism is the equilibrium bootstrap current density modified by the presence of the island [57] while the finite value of the heat conductivity parallel to the magnetic field line has a stabilizing effect on islands with small width as well as the polarization current density. As the island induced bootstrap current density is included in the derivation of the island evolution equation, there is a lower limit on the absolute value of $|\Delta'|$ for the island to be unstable:

$$|r_s\Delta'| > |r_s\Delta_c'| = 1.2\beta_p\sqrt{\varepsilon\nu_{*e}^{-1}F(\varepsilon,\nu_{*e})}L_q/L_p$$

, where β_p is the poloidal beta, ν_{*e} is the electron collisionality parameter, and the form factor $F(\varepsilon,\nu_{*e})$ is used to take into account the effects of finite aspect ratio and ν_{*e} on the equilibrium bootstrap current density. This Δ_c' depends on the local value of β_p. If β_p is high enough, namely, the inequality sign is reversed, the magnetic island can be stabilized. This points to alternative routes to stabilize

the islands by increasing local β_p, or by tailoring the current density profile to modify Δ'.

4.2. Comparison of Δ' with Δ'_c for stable and unstable discharges of tearing mode

Even though the calculated Δ' only for the ideal outer region is insufficient to get the mode growth rate [58], it is still useful to evaluate the tearing stability. As the larger Δ', it's easier to cause the TM instability in theoretical predictions. Here, first two unstable discharges with small Δ' in Figure 3.4 and a stable discharge with a similar Δ' are chosen in the steady-state hybrid discharges for comparison. Another example of stable discharge, #125469 is a typical hybrid discharge at relatively low β_N to check the applicability.

In Figure 4.1 for discharges with the (2,1) TM and Figure 4.2 for stable discharges without the (2,1) TM, the Δ' evolutions are represented for a time series of equilibria to show the relative trend and the difference between the unstable and the stable discharges. Both stable and unstable discharges show the analytical Δ'_c in similar range.

As shown in Figure 4.1, the Δ' calculated from PEST-III increases for the unstable discharges and this Δ' can exceed these Δ'_c for tearing destabilization before the mode onset. Here, it is interesting to note that the mode onset didn't coincide with the condition of $\Delta' > \Delta'_c$. When the modes appear experimentally, the

calculated Δ' slowly decays after the TM are set towards marginality. This apparently indicates some degree of self-stabilization (consistent with the saturation) by the mode itself as the island modifies the local current density profile. For the stable discharges in Figure 4.2, the calculated Δ' stays below Δ'_c.

The analysis for the mode growth rate by matching the solution from the inner resistive layer and the outer ideal region is left for a future work.

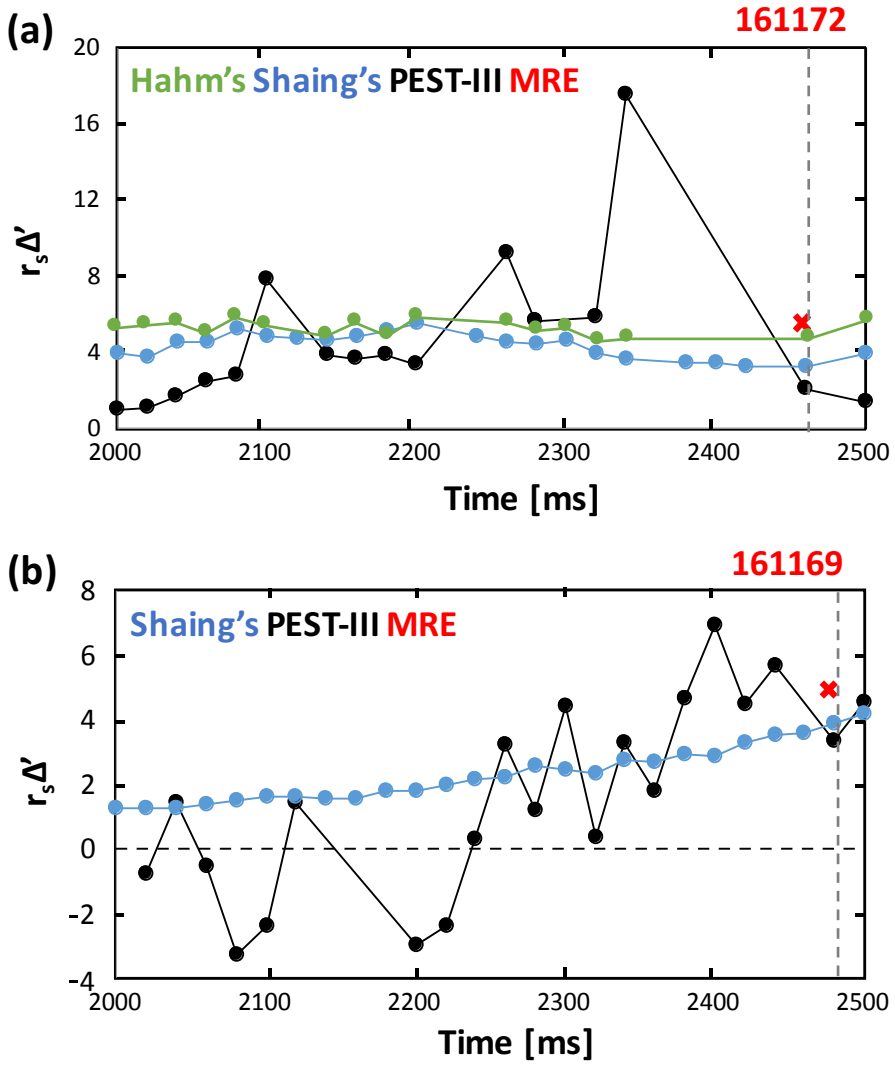

Figure 4.1 Evolution of the calculated $\Delta'_c r_s$ from analytical formula by Hahm's (green) and by Shaing's (blue), and $\Delta' r_s$ from PEST-III (black) and from MRE (red) on time series of equilibria for unstable discharges. (a) #161172 and (b) #161169. The vertical grey dashed line indicates the defined (2,1) TM onset.

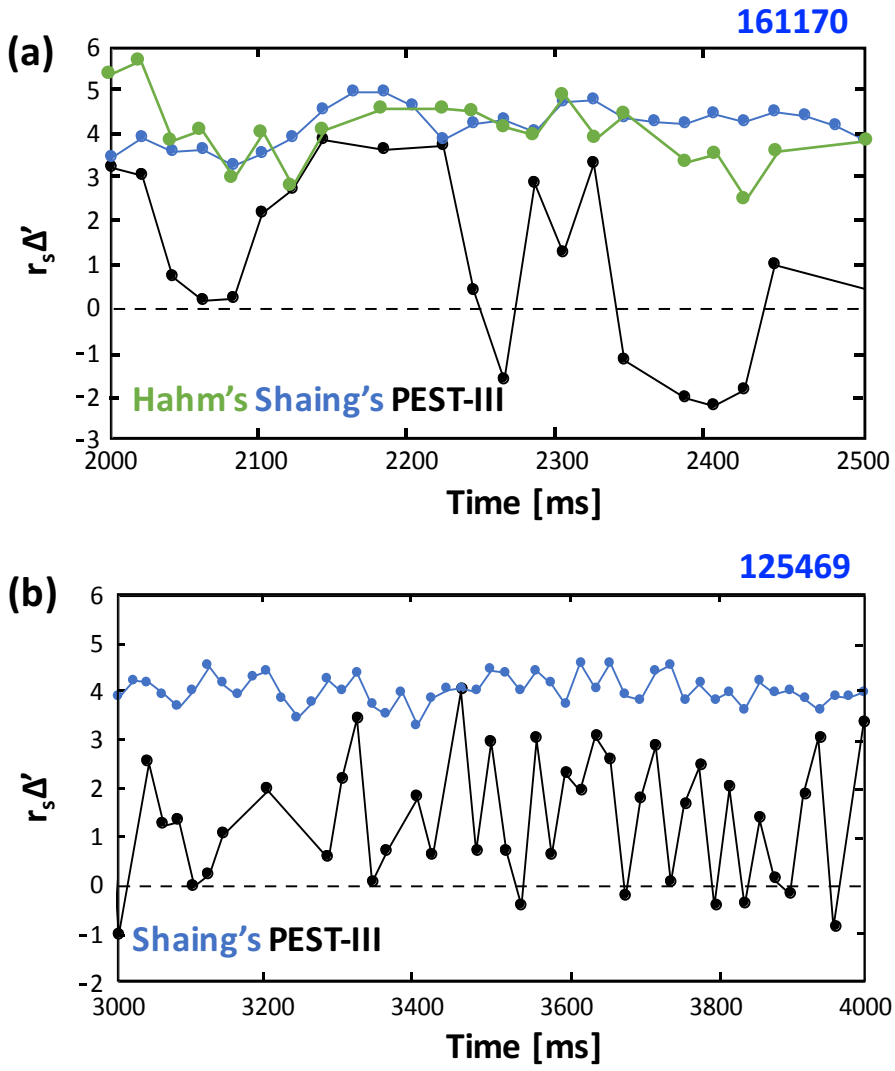

Figure 4.2 Evolution of the calculated $\Delta_c' r_s$ from analytical formula by Hahm's (green) and by Shaing's (blue), and $\Delta' r_s$ from PEST-III (black) on time series of equilibria for stable discharges. (a) #161170 and (b) #125469.

4.3. Estimation of Δ_c' from the extended MHD simulation

Instead of the analysis for the mode growth rate by matching the solution from the inner resistive layer and the outer ideal region, simulations with the NIMROD code (Non-Ideal Magnetohydrodynamics with Rotation, Open Discussion) [59] are performed for a preliminary study on the Δ_c' estimation from normalized mode growth rate $\gamma\tau_A$ where the linearized mode grows as $e^{\gamma t}$ in this thesis. The code maintains a certain degree of flexibility designed to study a variety of issues related to magnetic confinement.

NIMROD evolves the extended MHD fluid equations and the pre-Maxwell's equations (neglecting the displacement current) in 3D for fusion-relevant plasma parameters. The poloidal plane is represented using 2D spectral elements and the toroidal plane or out-of-plane is assumed to be periodic and is represented using finite Fourier series. This spatial representation is designed to efficiently model the complex poloidal cross-sections of modern day experiments, and it takes advantage of the toroidal symmetry present in many experiments. Mesh packing in the poloidal plane is used to ensure that regions of strong gradients are sufficiently resolved and the computing power is not wasted unnecessarily in regions with weak gradients. The convergence properties of the spectral elements aid in resolving extreme anisotropies that arise in magnetically confined plasmas and help enforce the magnetic divergence constraint. A leap-frog scheme advances the fields in time, and a semi-implicit operator is used in the velocity advance permitting

large time steps. NIMROD uses two coordinate systems based on the problem of interest: (X, Y, Z) for linear periodic systems and (R, Z, φ) for toroidal systems.

NIMROD decomposes the physical fields into steady-state components and time varying perturbed components. The steady-state components do not vary in the periodic direction and are assumed to be in force balance. This decomposition allows both time-dependent linear and nonlinear calculations. Linear calculations neglect terms that are the product of two or more perturbed quantities. The decomposition also improves numerical accuracy, especially when the perturbed quantities are smaller than the steady-state components.

To study for tearing stability by NIMROD, the simulation is performed with the experimental equilibrium reconstruction for the Lunquist number $S \equiv \tau_R/\tau_A \sim 1e^7$ with $(2,1)$ tear-type initial perturbation. The mode growth rate from NIMROD can be computed by plotting the slope of the natural logarithm of the magnetic energy, $\ln E_m$ and dividing this slope by 2 [60]. The $(2,1)$ tear-type initial perturbation has a positive growth rate for the unstable steady-state hybrid discharge in Figure 4.3 (a) and a negative growth rate for stable discharge in Figure 4.3 (b). At larger island size the island enters the Rutherford regime, where the island width increases algebraically, and the islands are visible with field line tracing as seen in Figure 4.4.

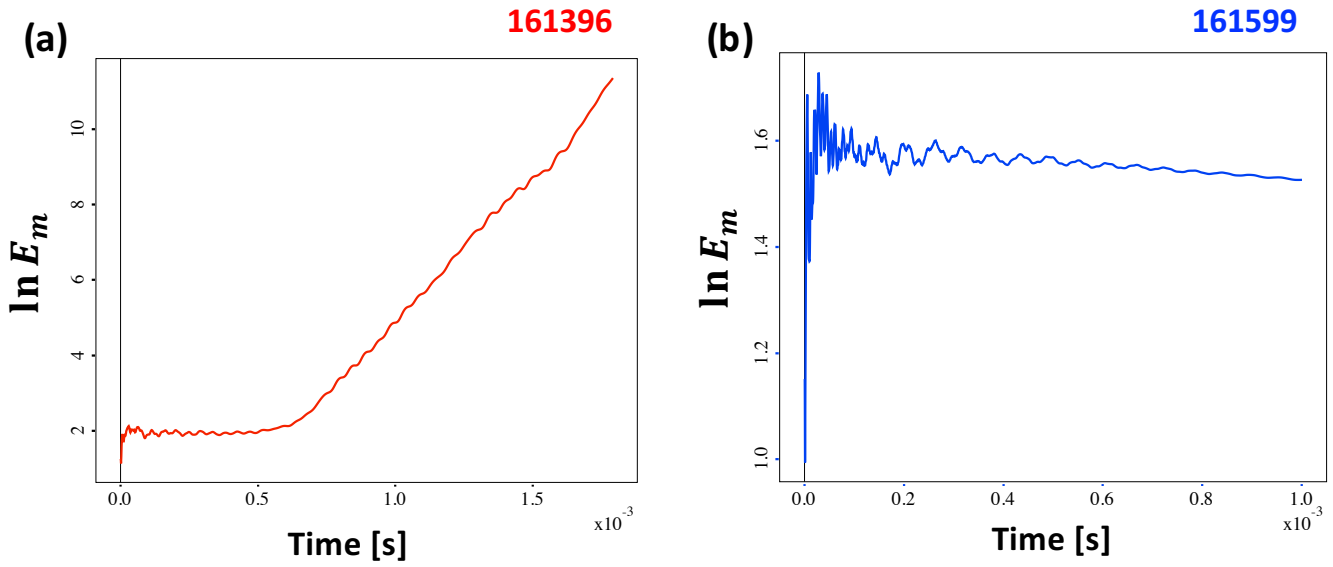

Figure 4.3 The natural logarithm of the magnetic energy mode $\ln E_m$ from NIMROD for the mode growth rate. (a) the discharge with (2,1) TM (#161396) and (b) the discharge without (2,1) TM (#161599).

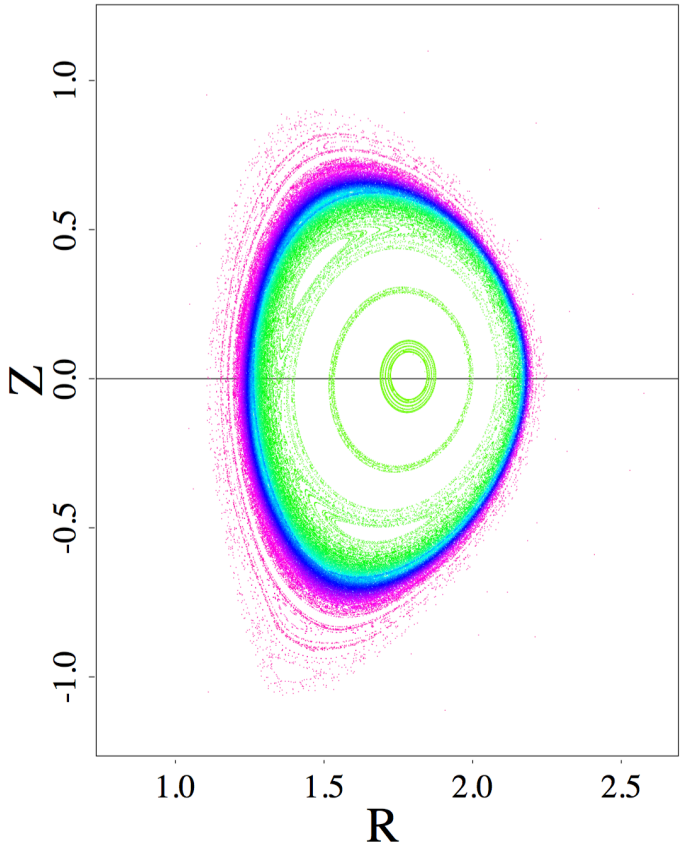

Figure 4.4 Poincaré plots of magnetic field lines traced during a simulation with (2,1) tear-type initial perturbation.

NIMROD simulations for the mode growth rate are performed using the various equilibria with the different Δ' as shown in Figure 4.5. The Δ'_c can be fitted for negative growth rate using the relation between the normalized mode growth rate $\gamma\tau_A$ from NIMROD and the Δ' from PEST-III. For the equilibria used in Figure 4.5, the Δ'_c is estimated as 3.5 by the linear fit between the normalized mode growth rate $\gamma\tau_A$ and the Δ' in Figure 4.6.

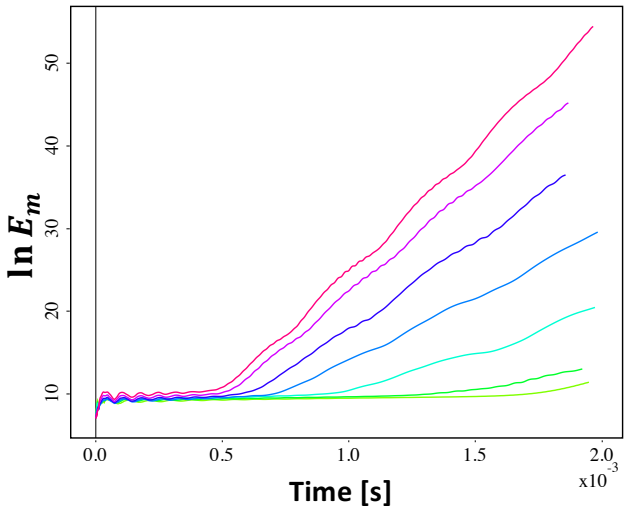

Figure 4.5 The natural logarithm of the magnetic energy mode $\ln E_m$ from NIMROD for the mode growth rate with various plasma equilibrium and profiles with different Δ'.

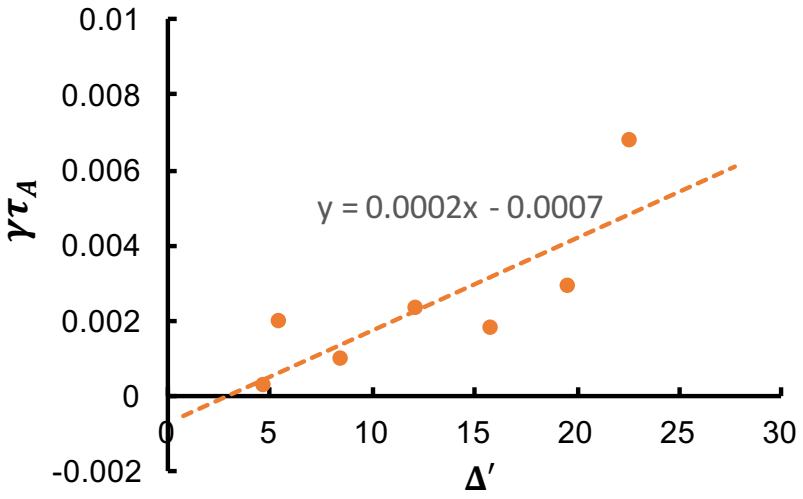

Figure 4.6 The Δ'_c estimation from the relation between the normalized mode growth rate $\gamma\tau_A$ and the Δ'.

Chapter 5.

Development of tearing mode onset model

Deleterious (2,1) TM appears in some steady-state hybrid scenario DIII-D discharges. The unstable discharge for (2,1) TM as shown as the example in this thesis is interpreted as due to an initially positive (destabilizing) classical tearing index Δ' calculated by PEST-III with the high quality of the equilibrium reconstruction in Chapter 2. However, the stable discharge with similar operation has also positive classical tearing index Δ', but smaller value than the unstable discharge. Since the good average curvature in a toroidal plasma and the polarization current can provide additional stabilizing influence on the stability of the tearing mode, the conventional wisdom of tearing instability criterion $\Delta' > 0$ can be modified $\Delta' > \Delta'_c > 0$. The critical parameter Δ'_c has been determined in various approaches with the different assumptions in Chapter 4.

In this chapter, the tearing mode onset model was introduced using the difference between Δ' and Δ'_c. Further, the plasma profile effects on tearing stability can be evaluated through the modeled equilibria.

5.1. Descriptions of tearing mode onset model

It is well known that the tearing instability in a tokamak is driven by the radial gradient of the equilibrium current density, and determined as the β limit. As shown in Figure 5.1, an integrated modeling package has been established to enable analysis of equilibria with parametric variations of the pressure or current profiles at the mode rational surface for determining the onset dependency on the

tearing stability index Δ'. The detailed procedure is as following. The reference profile was selected from an experiment at mode onset. A series of equilibria is constructed with ff' and p' from the given current or pressure profiles after varying parametrically by IPS/FASTRAN module. These modeled equilibria were analyzed via the asymptotic matching method using the PEST-III for Δ' and theoretical formula for Δ'_c [56]. Finally, the stability boundary for tearing mode onset is determined with L_p-L_q diagram using the difference between Δ' and Δ'_c.

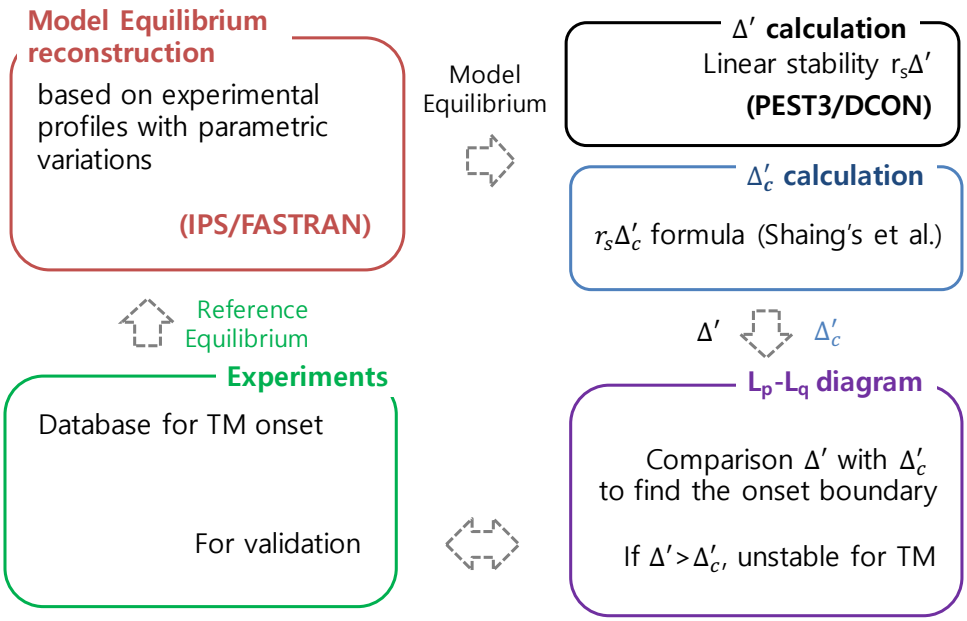

Figure 5.1 The overview of the procedure of the integrated modeling package for determining the tearing mode onset with current and pressure profile variations.

5.2. Construction of modeled equilibrium with the parametric variations

A series of equilibria was constructed that varied the gradient of the current or the pressure profile at the mode surface parametrically while minimizing the change of the global features such as l_i, the pressure peakness $f_p = p_0/\langle p \rangle$, and β_N based on the kinetic EFIT for the $(2,1)$ unstable discharge at the onset as the reference.

Proper choice of the functions and boundary conditions to vary the current or the pressure profile is crucial to accurately analyze the dependence of Δ' on these profile variations, as well as to reconstruct the equilibrium with reasonable convergences. In this thesis, the sine function was considered to apply the local variation at the mode surface within $[\rho_s - \delta,\ \rho_s + \delta]$ as the domain. Here, ρ_s is the mode surface and δ is the distance between the mode surface and the edge bootstrap boundary for equilibrium reconstruction. The perturbed profile and its first derivative should be continuous at the boundary of the domain and the total plasma current were kept a constant. Figure 5.2 shows the variations of the current density profile and the pressure profile of the modeled equilibria.

Another set of equilibria as reference was generated that increased the pressure multiplicatively to evaluate the Δ' dependence on $f_p = p_0/\langle p \rangle$ and β_N while conserving the safety factor profile as shown in Figure 5.3. It is noteworthy that l_i is not varied since the shape of current profile is similar in most hybrid scenarios and its variation easily makes the plasma ideally unstable.

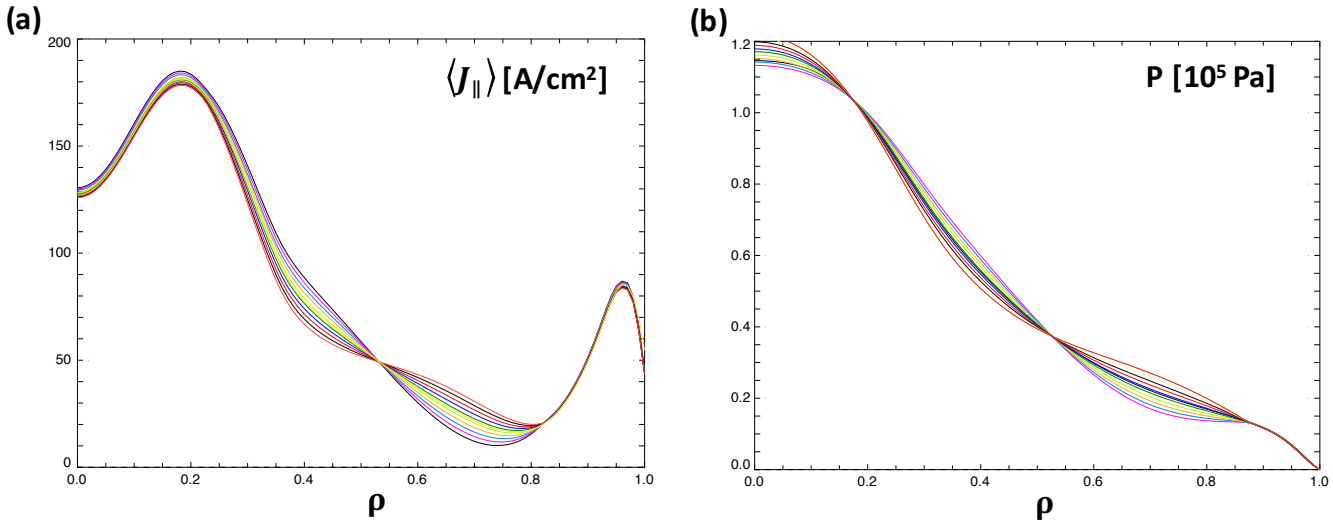

Figure 5.2 The plasma profiles of modeled equilibria based on the experiment with parametric variation at the mode surface, (a) the current density profile and (b) the pressure profile.

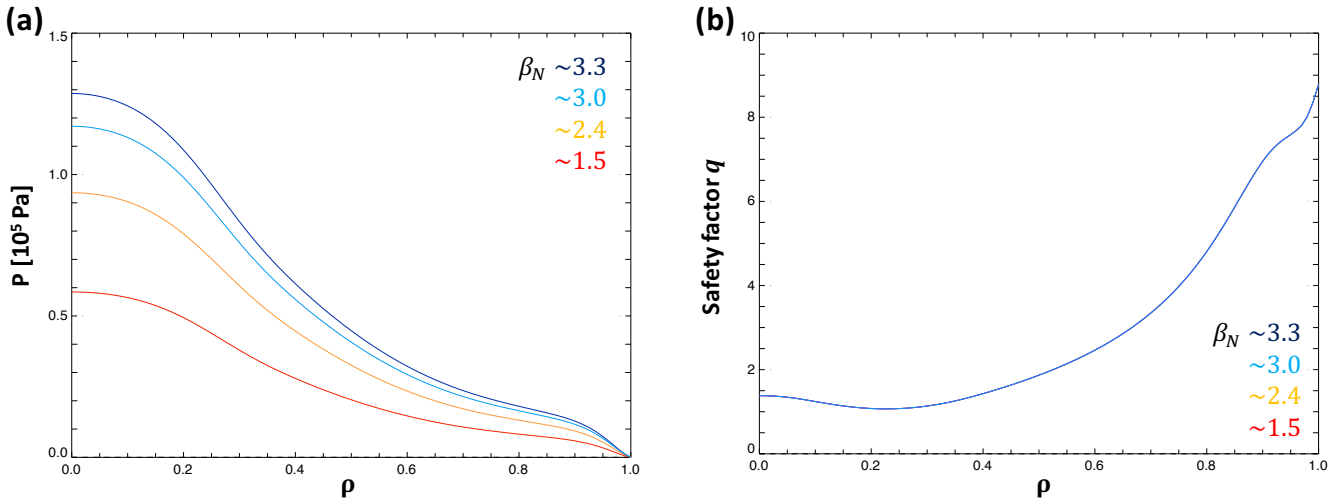

Figure 5.3 The plasma profiles of modeled equilibria with β_N variations, (a) the pressure profile as the reference and (b) the corresponding safety factor profile.

5.3. Stability boundary for tearing mode onset on L_p-L_q diagram

The stability diagram for tearing mode mapped on L_p-L_q parameter space using the difference between the Δ' calculated from PEST-III and the analytical formula Δ'_c. Since the safety factor profile $q(\psi)$ is correlated to the current density profile $J(\psi)$, the tearing stability diagram is cast in terms of two local parameters, such as the magnetic shear length L_q and the pressure scale length L_p.

The stability diagram can be characterized by the calculated Δ' rather than the analytical Δ'_c since the analytical Δ'_c is proportional to L_q/L_p by the definition (see Figure 5.4). Figure 5.5 shows the stability diagram calculated using a series of modeled equilibria from the variated plasma current and pressure profiles in Figure 5.2. Two experimental results are overlapped onto the stability diagram; one is with $(2,1)$ TM at onset and the other is without $(2,1)$ TM. It is shown that the $(2,1)$ TM onset is near the stability boundary while the $(2,1)$ stable discharge lies in the stable region in Figure 5.5. Both have similar L_p but different L_q which implies that the tearing instability is mainly driven by the radial gradient of the equilibrium current density. It is interesting to note that the tearing stability is more stable as the radial gradient of the pressure profile increases.

It is important to keep in mind, however, that the tearing stability is not local. In general, the shape of the profiles throughout the pedestal region and into the core impacts the tearing stability.

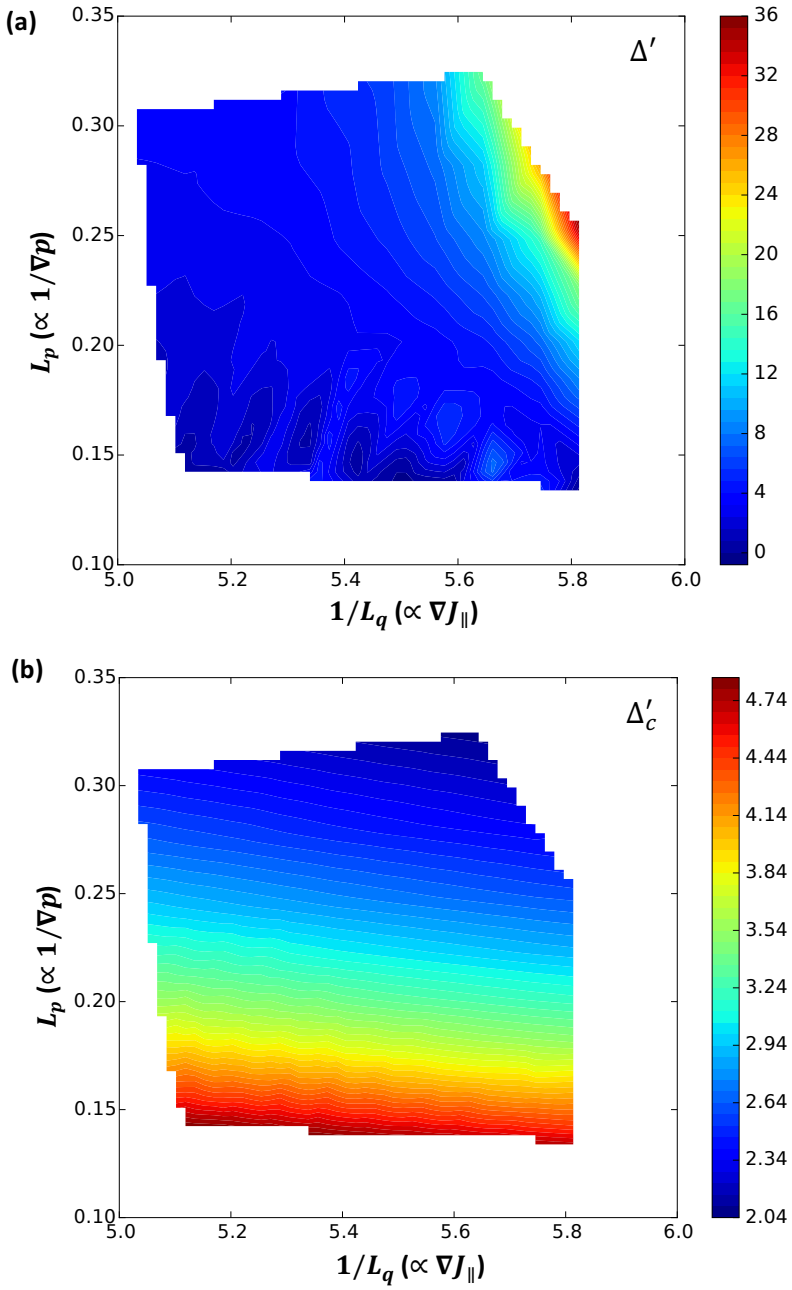

Figure 5.4 The stability diagram for tearing mode on L_p-L_q parameter space using (a) the tearing stability index Δ' and (b) the critical tearing stability index Δ'_c

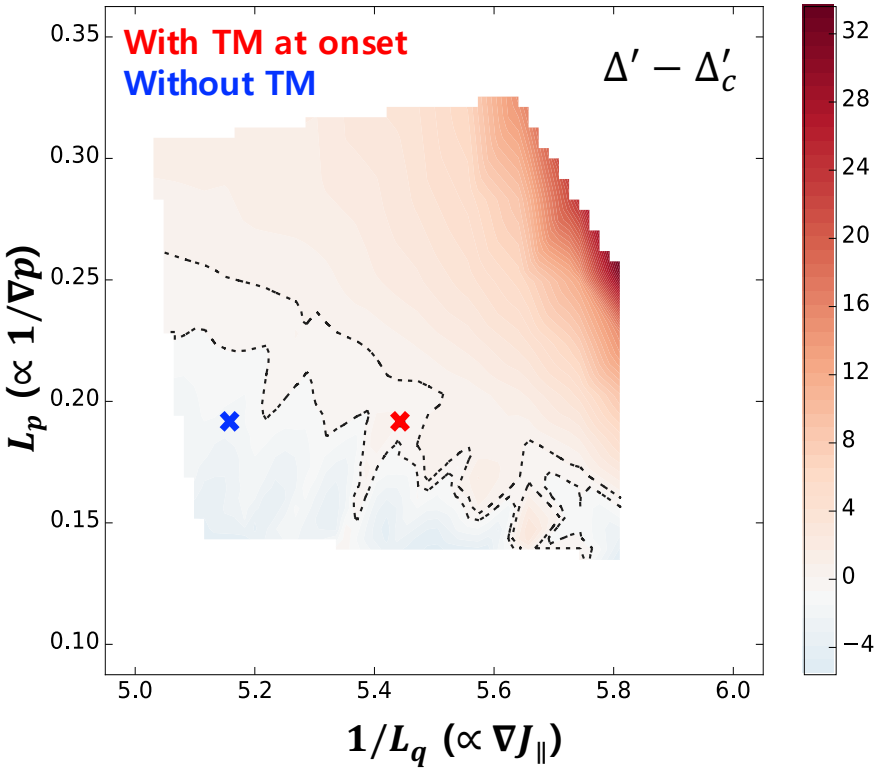

Figure 5.5 The stability diagram for tearing mode on L_p-L_q parameter space using the difference between the Δ' and the Δ'_c. The black dashed line pointed out the marginal condition as $\Delta' = \Delta'_c$. The red point is the discharge with TM at onset (#161172) and the blue point is the discharge without TM (#161170).

The stability diagrams for TM onset for various β_N are shown in Figure 5.6. As β_N increases, the instability window of $\Delta' > \Delta'_c$ becomes wider as well as the absolute value of $\Delta' - \Delta'_c$ also increases. If β_N is further increased, whole region on the stability diagram becomes unstable. These results indicate that the tearing mode occurs easier at high β_N regardless of the profile features based on this reference shape. Although the safety factor profile is fixed, the ideal unstable region also tends to expand. The open circles indicate the experimental points at (2,1) TM onset for each β_N in the Figure 5.6. The (2,1) TM is observed to appear when the profiles reach near the marginal area, $\Delta' \sim \Delta'_c$. The stability boundary ($\Delta' = \Delta'_c$) of Figure 5.6 are presented in Figure 5.7.

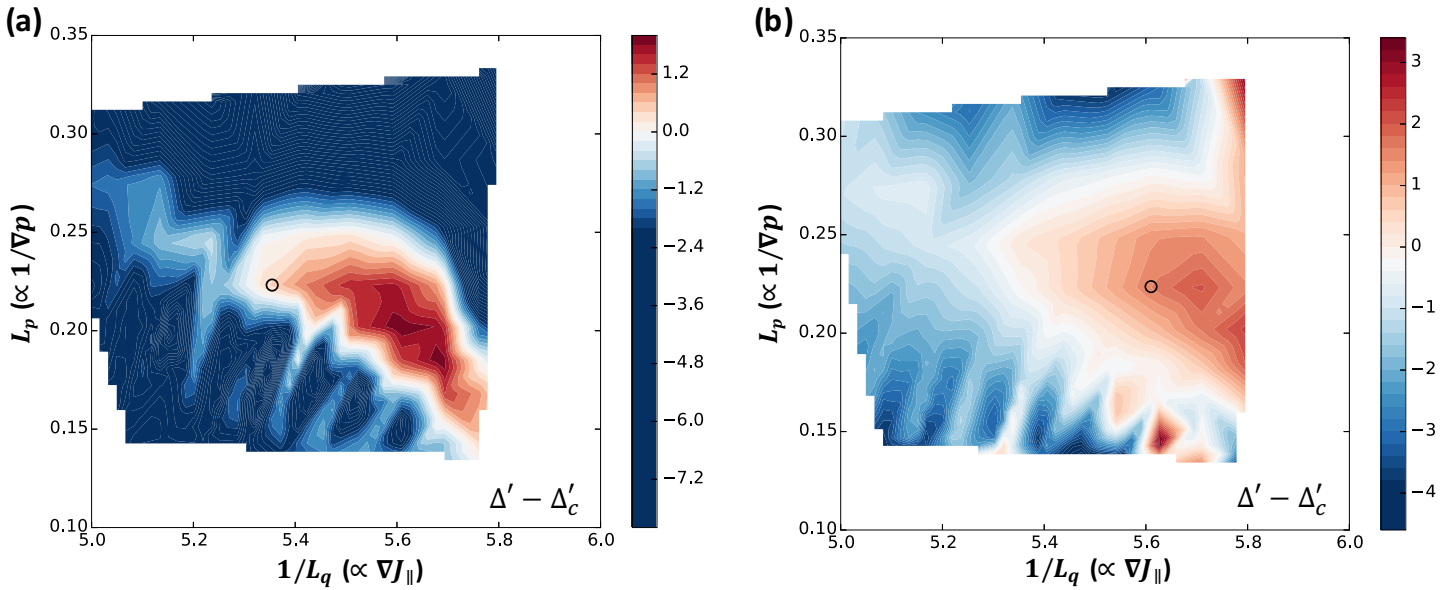

Figure 5.6 The stability diagram for tearing mode on L_p-L_q parameter space with various β_N, (a) β_N~1.5, (b) β_N~2.4, (c) β_N~3.0, and (d) β_N~3.3. The blue indicates stable ($\Delta' < \Delta'_c$) and the red indicates unstable ($\Delta' > \Delta'_c$) for (2,1) TM stability. The black open circle indicates the experimental data at (2,1) TM onset.

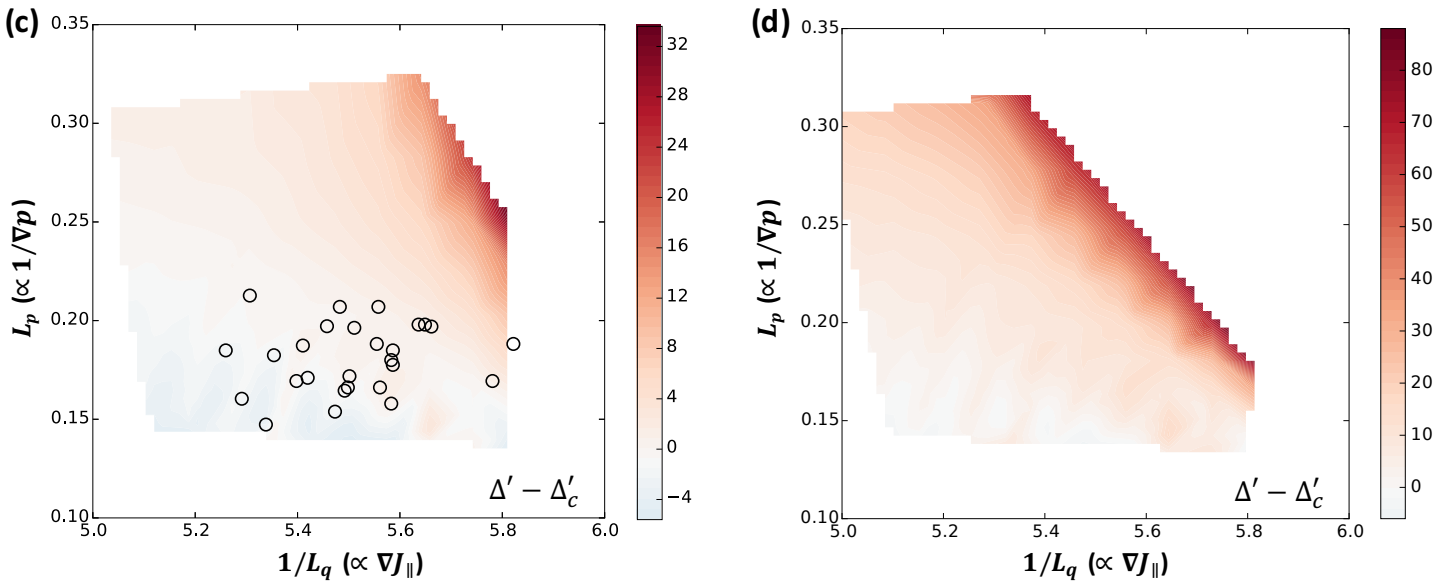

Figure 5.6 The stability diagram for tearing mode on L_p-L_q parameter space with various β_N, (a) β_N~1.5, (b) β_N~2.4, (c) β_N~3.0, and (d) β_N~3.3. The blue indicates stable ($\Delta' < \Delta'_c$) and the red indicates unstable ($\Delta' > \Delta'_c$) for (2,1) TM stability. The black open circle indicates the experimental data at (2,1) TM onset. (continued)

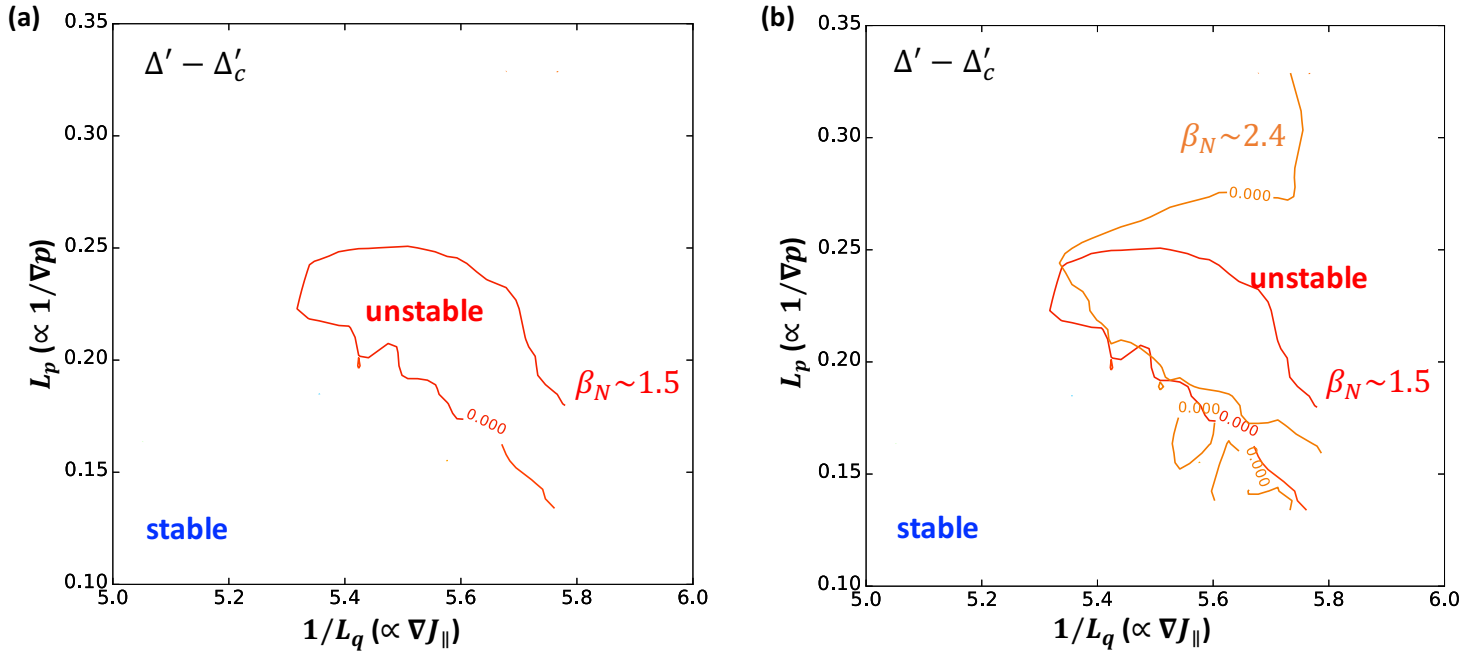

Figure 5.7 The stability boundary ($\Delta' = \Delta'_c$) for tearing mode onset on L_p-L_q parameter space according to β_N, (a) β_N~1.5 only (red), (b) β_N~2.4 (orange), (c) β_N~2.7 (green) and β_N~3.0 (light blue shade), and (d) β_N~3.3 (dark blue).

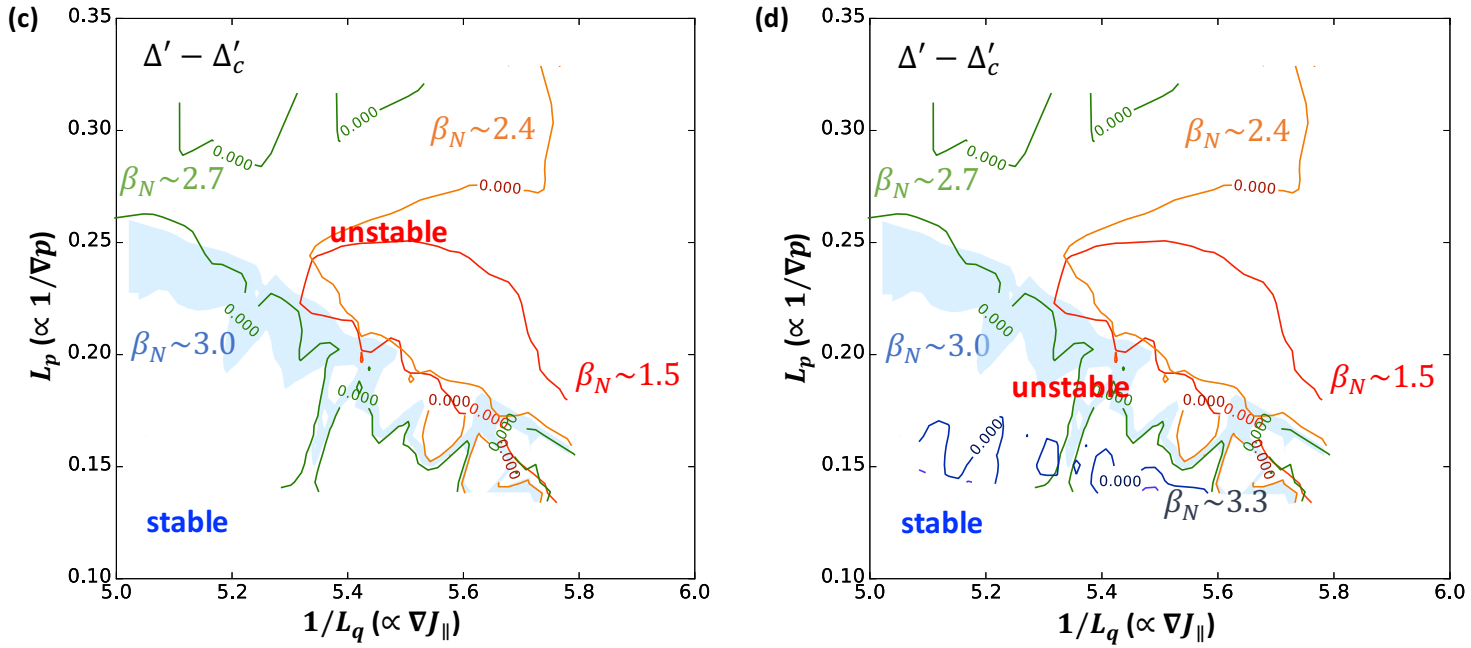

Figure 5.7 The stability boundary ($\Delta' = \Delta'_c$) for tearing mode onset on L_p-L_q parameter space according to β_N, (a) β_N~1.5 only (red), (b) β_N~2.4 (orange), (c) β_N~2.7 (green) and β_N~3.0 (light blue shade), and (d) β_N~3.3 (dark blue). (continued)

Chapter 6.

Conclusions

6.1. Summary and concluding remarks

Tearing modes (TMs) can significantly degrade confinement and set a limit on achievable plasma beta. It is important to understand the onset threshold and the evolution of TMs for developing a high-performance steady state fusion reactor. Based on the steady-state hybrid experiments performed on the DIII-D device, the occurrence of TM is identified and analyzed, and the relationship between the plasma current and the pressure profiles on the tearing stability in terms of the tearing stability index Δ' is investigated.

Firstly, the characteristics of the mode is mainly investigated using the system of magnetic pick-up Mirnov probes. The mode onset, the mode amplitude, and the mode number is identified by the FFT analysis and the phase-fitting method. Especially, the mode onset is defined at the time without the phase-folding of the magnetic signals for this thesis.

Secondly, a more accurate and tightly constrained equilibrium is reconstructed using the well-measured plasma profiles using various diagnostics. Since the tearing stability is sensitive to the equilibrium current and pressure profiles, it is performed iteratively until the convergence is reached.

The characteristics of plasma current and pressure profiles at tearing mode onset in the database of DIII-D steady-state hybrid discharges were determined by representative parameters such as the internal inductance l_i, the plasma pressure peaking factor $f_p = p_0/\langle p \rangle$, the magnetic shear length $L_q = q/(dq/dr)$, the

pressure gradient length $L_p = -p/(dp/dr)$ and the local resistive diffusion time τ_R. The (2,1) TM onset seems to be more sensitive to the global feature of plasma profile through l_i and f_p, and the effect of plasma resistivity at the mode surface through τ_R than the local feature of plasma profile through L_q and L_p. However, the local feature of plasma profile cannot be ignored when the normalized β_N at (2,1) TM onset is fitted in terms of these five plasma parameters. From the result of the best fit equation in the dimensionless form using r_s and τ_A, the global feature of profiles and the current profile can affect more than the local feature of profiles and the pressure profile, respectively.

Thirdly, the tearing stability index Δ' is calculated with the experimental equilibria in two ways, by MHD codes (PEST3 and resistive DCON) and by MRE. Numerical Δ' by MHD code is calculated as the outer solution from the Δ' definition and experimental estimation of Δ' by MRE included the effects of the bootstrap current and the ion polarization current in this thesis. They are verified and validated in reasonable agreement. It is noteworthy that the determined Δ' can be positive regardless of the mode onset, so the conventional wisdom of $\Delta' > 0$ for tearing destabilization may not be the sufficient condition, rather a positive value greater than a certain threshold could replace this under the toroidal geometry.

Fourthly, the analytical formula of the tearing stability threshold Δ'_c is reviewed for the semi-collisional regime and the collisionless banana regime. By comparing the analytical Δ'_c with the Δ' calculated from PEST-III code near the

TM onset, it is found that the condition of $\Delta' > \Delta'_c$ is required for the mode onset in the experiment. A preliminary study on the Δ'_c estimation from the normalized mode growth rate is performed by NIMROD code. The Δ'_c can be fitted for negative or marginal growth rate using the relation between the normalized mode growth rate $\gamma\tau_A$ from NIMROD and the Δ' from PEST-III.

Finally, a stability diagram of $n = 1$ tearing mode onset is suggested with local and global features of plasma profiles. Onset condition of $n = 1$ TM is analyzed by the difference between Δ' and Δ'_c, and its stability diagram is derived in terms of the local ($\nabla J_{\parallel}$ and ∇p) and global (β_N) variations for steady-state hybrid scenarios. To calculate $\Delta' - \Delta'_c$ for the stability diagram, a novel modeling package has been developed by integrating IPS/FASTRAN for equilibrium reconstruction, PEST-III/DCON for linear stability Δ' calculation, and the Δ'_c solver for analytical Δ'_c calculation. The stability boundary at the mode onset, $\Delta' = \Delta'_c$, is mapped on L_p-L_q diagram. Characteristics of this stability boundary show that the TM unstable area expands, then the stability boundary moves as β_N increases. This stability diagram can be used to design and control experiments to avoid $n = 1$ TM.

6.2. Recommendations for future work

Future wok will be focused on further improvements of the method and the validation with the various experiments.

The stability diagram for TM mapped in this thesis is firstly suggested for the onset prediction. More general stability diagram can be pursued by expanding the database of the reference equilibrium and by applying the various perturbed function.

This stability diagram can be validated systematically by conducting the dedicated experiments or datamining the experiments. It might be required to distinguish or separate the correlation between the local and global characteristics of profiles.

The stability boundary can be verified with zero growth rate boundary calculated by non-linear MHD code such as NIMROD and better formulas of which would be applicable to the future reactor can be explored on the stability diagram.

BIBLIOGRAPHY

[1] A. Einstein, Does the Inertia of a Body Depend upon its Energy Content?, *Annalen der Physik* **323**, 639 (1905).

[2] W. M. Stacey, "An Introduction to the Physics and Technology of Magnetic Confinement", John Wiley & Sons, Inc, New York, 1984.

[3] J. Raeder, K. Borrass, R. Bunde, W. Danner, R. Klingelhofer, L. Lengyel, F. Leuterer, M. Soll, "Controlled Nuclear Fusion", John Wiley & Sons, Inc, New York, 1986.

[4] M. Kikuchi, et al., "Fusion Physics", International Atomic Energy Agency, Vienna, 2012.

[5] ENDF database at the IAEA: http://www-nds.iaea.org/exfor/e4explorer.htm.

[6] NRL Plasma Formulary.

[7] Eurofusion Organization, "Tokamak Principle": https://www.euro-fusion.org/2011/09/tokamak-principle-2/?view=gallery-11.

[8] J. Luxon, A design retroscpetive of the DIII-D tokamak, *Nucl. Fusion* **42**, 614 (2002).

[9] H. Zohm, Magnetohydrodynamic Stability of Tokamaks, Wiley-VCH, 2015.

[10] C. Kessel, J. Manickam, G. Rewoldt, and W.M. Tang, Improved plasma performance in tokamaks with negative magnetic shear, *Phys. Rev. Lett.* **72**, 1212 (1994).

[11] A.C.C. Sips, for the Steady State Operation, and the Transport Physics topical groups of the International Tokamak Physics Activity, Advanced scenarios for ITER operation, *Plasma Phys. Contr. Fusion* **47**, A19 (2005).

[12] E.J. Strait, L.L. Lao, M.E. Mauel, B.W. Rice, T.S. Taylor, K.H. Burrell, M.S. Chu, E.A. Lazarus, T.H. Osborne, S.J. Thompson, and A.D. Turnbull, Enhanced Confinement and Stability in DIII-D Discharges with Reversed Magnetic Shear, *Phys. Rev. Let.* **75**, 4421 (1995).

[13] F.M. Levinton, M.C. Zarnstorff, S.H. Batha, M. Bell, R.E. Bell, R.V. Budny, C. Bush, Z. Chang, E. Fredrickson, A. Janos, J. Manickam, A. Ramsey, S.A. Sabbagh, G.L. Schmidt, E.J. Synakowski, and G. Taylor, Improved confinement with reversed magnetic shear in TFTR, *Phys. Rev. Let.* **75**, 4417 (1995).

[14] R.C. Wolf, O. Gruber, M. Maraschek, R. Dux, C. Fuchs, S. Günter, A. Herrmann, A. Kallenbach, K. Lackner, P.J. McCarthy, H. Meister, G. Pereverzev, J. Schweinzer, U. Seidel and the ASDEX Upgrade Team, Stationary advanced scenarios with internal transport barrier on ASDEX Upgrade, *Plasma Phys. Contr. Fusion* **41**, B93 (1999).

[15] T.C. Luce, M.R. Wade, P.A. Politzer, S.L. Allen, M.E. Austin, D.R. Baker, B. Bray, D.P. Brennan, K.H. Burrell, T.A. Casper, M.S. Chu, J.C. DeBoo, E.J. Doyle, J.R. Ferron, A.M. Garofalo, P. Gohil, I.A. Gorelov, C.M. Greenfield, R.J. Groebner, W.W. Heidbrink, C.-L. Hsieh, A.W. Hyatt, R. Jayakumar, J.E. Kinsey, R.J. La Haye, L.L. Lao, C.J. Lasnier, E.A. Lazarus, A.W. Leonard, Y.R. Lin-Liu, J. Lohr, M.A. Mahdavi, M.A. Makowski, M. Murakami, C.C. Petty, R.I. Pinsker, R. Prater, C.L. Rettig, T.L. Rhodes, B.W. Rice, E.J. Strait, T.S. Taylor, D.M. Thomas, A.D. Turnbull, J.G. Watkins, W.P. West and K.-L. Wong, Long pulse high performance discharges in the DIII-D tokamak, *Nucl. Fusion* **41**, 1585 (2001).

[16] A.C.C. Sips, Steady state advanced scenarios at ASDEX Upgrade, *Plasma Phys. Contr. Fusion* **44**, B69 (2002).

[17] M.R. Wade, T.C. Luce, P.A. Politzer, J.R. Ferron, S.L. Allen, M.E. Austin, D.R. Baker, B. Bray, D.P. Brennan, K.H. Burrell, T.A. Casper, M.S. Chu, J.C. DeBoo, E.J. Doyle, A.M. Garofalo, P. Gohil, I.A. Gorelov, C.M. Greenfield, R.J. Groebner, W.W. Heidbrink, C.L. Hsieh, A.W. Hyatt, R.J. Jayakumar, J.E. Kinsey, R.J. La Haye, L.L. Lao, C.J. Lasnier, E.A. Lazarus, A.W. Leonard, Y.R. Lin-Liu, J. Lohr, M.A. Mahdavi, M.A. Makowski, M. Murakami, C.C. Petty, R.I. Pinsker, R. Prater, C.L. Rettig, T.L. Rhodes, B.W. Rice, E.J. Strait, T.S. Taylor, D.M. Thomas, A.D. Turnbull, J.G. Watkins, W.P. West, and K.L. Wong, Progress toward long-pulse high-performance Advanced Tokamak discharges on the DIII-D tokamak, *Phys. Plasmas* **8**, 2208 (2001).

[18] T.C. Luce, Development of Steady-State Advanced Tokamak Research in the DIII-D Tokamak, *Fusion Sci. Technol.* **48**, 1212 (2005).

[19] C.T. Holcomb, W.W. Heidbrink, J.R. Ferron, M.A. Van Zeeland, A.M. Garofalo, W.M. Solomon, X. Gong, D. Mueller, B.A. Grierson, E.M. Bass, C. Collins, J.M. Park, K. Kim, T.C. Luce, F. Turco, D.C. Pace, Q. Ren, and M. Podesta, Fast-ion transport in $q_{min}>2$, high-β steady-state scenarios on DIII-D, *Phys. Plasmas* **22**, 055904 (2015).

[20] J.R. Ferron, C.T. Holcomb, T.C. Luce, J.M. Park, E. Kolemen, R.J. La Haye, W.M. Solomon, and F. Turco, High internal inductance for steady-state operation in ITER and a reactor, *Nucl. Fusion* **55**, 073030 (2015).

[21] F. Turco, C.C. Petty, T.C. Luce, T.N. Carlstrom, M.A. Van Zeeland, W. Heidbrink, F. Carpanese, W. Solomon, C.T. Holcomb, and J.R. Ferron, The high-β_N hybrid

scenario for ITER and FNSF steady-state missions, *Phys. Plasmas* **22**, 056113 (2015).

[22] C.C. Petty, J.E. Kinsey, C.T. Holcomb, J.C. DeBoo, E.J. Doyle, J.R. Ferron, A.M. Garofalo, A.W. Hyatt, G.L. Jackson, T.C. Luce, M. Murakami, P.A. Politzer, and H. Reimerdes, High-beta, steady-state hybrid scenario on DIII-D, *Nucl. Fusion* **56**, 016016 (2016).

[23] M.R. Wade, T.C. Luce, R.J. Jayakumar, P.A. Politzer, A.W. Hyatt, J.R. Ferron, C.M. Greenfield, M. Murakami, C.C. Petty, R. Prater, J.C. DeBoo, R.J. La Haye, P. Gohil, and T.L. Rhodes, Development, physics basis and performance projections for hybrid scenario operation in ITER on DIII-D, *Nucl. Fusion* **45**, 407 (2005).

[24] C.C. Petty, R.J. La Haye, T.C. Luce, D.A. Humphreys, A.W. Hyatt, J. Lohr, R. Prater, E.J. Strait, and M.R. Wade, Hybrid Regime as an Alternative Scenario for High-Beta, Steady State Plasmas, *Nucl. Fusion* **44**, 243 (2004).

[25] C.C. Petty, M.E. Austin, C.T. Holcomb, R.J. Jayakumar, R.J. La Haye, T.C. Luce, M.A. Makowski, P.A. Politzer, and M.R. Wade, Magnetic-Flux Pumping in High-Performance, Stationary Plasmas with Tearing Modes, *Phys. Rev. Let.* **102**, 045005 (2009).

[26] F. Turco, C.T. Holcomb, J.R. Ferron, T.C. Luce, P.A. Politzer, J.M. Park, A.E. White, D.P. Brennan, A.D. Turnbull, J.M. Hanson, M. Okabayashi, and Y.K. In, Sensitivity of transport and stability to the current pro le in steady-state scenario plasmas in DIII-D, *Phys. Plasmas* **19**, 122506 (2012).

[27] O. Sauter, R.J. La Haye, Z. Chang, D.A. Gates, Y. Kamada, H. Zohm, A. Bondeson, D. Boucher, J.D. Callen, M.S. Chu, T.A. Gianakon, O. Gruber, R.W. Harvey, C.C. Hegna, L.L. Lao, D.A. Monticello, F.W. Perkins, A. Pletzer, A. Reiman, M.N. Rosenbluth, E.J. Strait, T.S. Taylor, A.D. Turnbull, F.L. Waelbroeck, J.C. Wesley, H.R. Wilson, and R. Yoshino, Beta limits in long-pulse tokamak discharges, *Phys. Plasmas* **4**, 1654 (1997).

[28] D.P. Brennan, E.J. Strait, A.D. Turnbull, M.S. Chu, R.J. La Haye, T.C. Luce, T.S. Taylor, S. Kruger, and A. Pletzer, Tearing mode stability studies near ideal stability boundaries in DIII-D, *Phys. Plasmas* **9**, 2998 (2002).

[29] D.P. Brennan, R.J. La Haye, A.D. Turnbull, M.S. Chu, T.H. Jensen, L.L. Lao, T.C. Luce, P.A. Politzer, E.J. Strait, S. Kruger, and D.D. Schnack, A mechanism for tearing onset near ideal stability boundaries, *Phys. Plasmas* **10**, 1643 (2003).

[30] R.J. La Haye, P.A. Politzer, and D.P. Brennan, Beta limit due to m/n= 2/1 tearing mode onset in the DIII-D hybrid scenario, *Nucl. Fusion* **48**, 015005 (2008).

[31] H.P. Furth, P.H. Rutherford, and H. Selberg, Tearing mode in the cylindrical tokamak, *Phys. Fluids* **16**, 1054 (1973).

[32] H.P. Furth, J. Killeen, and M.N. Rosenbluth, Finite-resistivity instabilities of a sheet pinch, *Phys. Fluids* **6**, 456 (1963).

[33] P. H. Rutherford, Nonlinear growth of the tearing mode, *Phys. Fluids* **16**, 1903 (1973)

[34] V. Igochine, "Active Control of Magneto-hydrodynamic Instabilities in Hot Plasmas", Springer, 2015.

[35] J.R. Ferron and E.J. Strait, Real time analysis of tokamak discharge parameters, *Rev. Sci. Instrum.* **63**, 4799 (1992).

[36] E.J. Strait, Magnetic diagnostic system of the DIII-D tokamak, *Rev. Sci. Instrum.* **77**, 023502 (2006).

[37] J.S. Kim, D.H. Edgell, J.M. Greene, E.J. Strait and M.S. Chance, MHD mode identification of tokamak plasmas from Mirnov signals, *Plasma Phys. Control. Fusion* **41**, 1399 (1999).

[38] R.J. La Haye, R.J. Buttery, S. Guenter, G.T.A. Huysmans, M. Maraschek, and H.R. Wilson, Dimensionless scaling of the critical beta for onset of a neoclassical tearing mode, *Phys. Plasmas* **7**, 3349 (2000).

[39] K.E.J. Olofsson, J.M. Hanson, D. Shiraki, F.A. Volpe, D.A. Humphreys, R.J. La Haye, M.J. Lanctot, E.J. Strait, A.S. Welander, E. Kolemen, and M Okabayash, Array magnetics modal analysis for the DIII-D tokamak based on localized time-series modelling, *Plasma Phys. Control. Fusion* **56**, 095012 (2014).

[40] L.L. Lao, H.St. John, R.D. Stambaugh and W. Pfeiffer, Separation of $\overline{\beta_p}$ and l_i in tokamaks of non-circular cross-section, *Nucl. Fusion* **25**, 1611 (1985).

[41] L.L. Lao, H.E.St. John, Q. Peng, J.R. Ferron, E.J. Strait, T. S. Taylor, W. H. Meyer, C. Zhang, and K.-I. You, MHD Equilibrium Reconstruction in the DIII-D Tokamak, *Fusion Sci. Technol.* **48**, 968 (2005).

[42] A.K. Cline, Six subprograms for curve fitting using splines under tension, *Commun. ACM* **17**, 218 (1974).

[43] A. Pankin, D. McCuneb, R. Andreb, G. Batemana, and A. Kritza, The tokamak Monte Carlo fast ion module NUBEAM in the National Transport Code Collaboration library, *Comput. Phys. Commun.* **159**, 157 (2004).

[44] W.W. Pfeiffer , R.H. Davidson , R.L. Miller and R.E. Waltz, "ONETWO: A computer code for modeling plasma transport in tokamaks", General Atomics Company Report, no. GA-A16178 (1980).

[45] C.C. Hegna and J.D. Callen, Stability of tearing modes in tokamak plasmas, *Phys. Plasmas* **1**, 2308 (1994).

[46] A. Pletzer and R.L. Dewar, Non-ideal stability: variational method for the determination of the outer-region matching data, *J. Plasma Phys.* **45**, 427 (1991).

[47] A. Pletzer, A. Bondeson, and R.L. Dewar, Linear Stability of Resistive MHD Modes: Axisymmetric Toroidal Computation of the Outer Region Matching Data, *J. Comput. Phys.* **115**, 530 (1994).

[48] R.L. Dewar and A. Pletzer, Two-dimensional generalizations of the Newcomb equation, *J. Plasma Phys.* **43**, 291 (1990).

[49] A.H. Glasser, The direct criterion of Newcomb for the ideal MHD stability of an axisymmetric toroidal plasma, *Phys. Plasmas* **23**, 072505 (2016).

[50] L.L. LoDestro and L.D. Pearlstein, On the Grad–Shafranov equation as an eigenvalue problem, with implications for q solvers, *Phys. Plasmas* **1**, 90 (1994).

[51] J. Crotinger, "Corsica: A comprehensive simulation of toroidal magnetic fusion devices", Lawrence Livermore National Laboratory Technical Report, No. UCRL-ID-126284 (1997).

[52] R.J. La Haye, Neoclassical tearing modes and their control, *Phys. Plasmas* **13**, 055501 (2006).

[53] R.J. La Haye, G.L. Jackson, T.C. Luce, K.E.J. Olofsson, W.M. Solomon and F. Turco, Insights into m/n=2/1 Tearing Mode Stability Based on Initial Island Growth Rate in DIII-D ITER Baseline Scenario Discharges, Proc. 41st EPS Conf. on Controlled Fusion and Plasma Physics, O5.134, Berlin, Germany (2014).

[54] A.H. Glasser, J.M. Greene, and J.L. Johnson, Resistive instabilities in general torioidal plasma configurations, *Phys. Fluids* **18**, 875 (1975).

[55] T.S. Hahm and L. Chen, Semicollisional drift-tearing modes in toroidal plasmas, *Phys. Fluids* **29**, 1891 (1986).

[56] K.C. Shaing and D.A. Spong, Magnetic island induced bootstrap current on island dynamics in tokamaks, *Phys. Plasmas* **13**, 022501 (2006).

[57] R. Carrera, R.D. Hazeltine, and M. Kotschenreuther, Island bootstrap current modification of the nonlinear dynamics of the tearing mode, *Phys. Fluids* **29**, 899 (1986).

[58] D.P. Brennan and L.E. Sugiyama, Resistive stability of 2/1 modes near 1/1 resonance *Phys. Plasmas* **13**, 052515 (2006).

[59] C.R. Sovinec, A.H. Glasser, T.A. Gianakon, D.C. Barnes, R.A. Nebel, S. Kruger, D.D. Schnack, S.J. Plimpton, A. Tarditi, and M.S. Chu, Nonlinear magneto hydrodynamics simulation using high-order finite elements, *J. Comput. Phys.* **195**, 355 (2004).

[60] T.A. Gianakon and S. Kruger, NIMROD and FAR Comparison for Tearing Modes in Tokamaks, Center for Plasma Theory and Computation Report, no.UW-CPTC 98-13 (1998).

ABSTRACT IN KOREAN

국 문 초 록

토카막 플라즈마에서 찢어짐 모드 (Tearing mode, TM) 불안정성 현상은 플라즈마의 성능을 제한하는 저항성 자기유체학적 불안정성의 한 종류이다. 이 현상에 대한 올바른 이해, 특히 찢어짐 모드의 발생 조건은 고성능 정상상태 운전을 위해 필수적이다. DIII-D 장치에서 수행된 정상상태 하이브리드 실험에 기초하여, 찢어짐 모드의 발생을 측정하고 그 특성을 분석하였으며, 찢어짐 모드 발생시의 플라즈마 전류 및 압력 분포와의 관계를 찢어짐 안정성 지표의 관점에서 확인하였다.

실험에서의 찢어짐 모드 발생 초기의 구조, 크기, 크기 증가율은 미르노프 자기 탐침 진단 (Mirnov probes)의 고속 푸리에 변환 (FFT) 분석과 위상 맞춤 분석을 통해 확인할 수 있다. 본 논문에서는 찢어짐 모드의 발생을 폴로이달 위상 맞춤 분석에서 위상 반전이 사라지는 순간으로 정의하여 연구를 진행하였다.

찢어짐 모드 안정성은 평형 전류와 압력 분포에 민감하므로, 실험에서 다양한 진단으로 측정된 플라즈마 분포를 이용하여 더 정확한 평형을 재구성하는 것이 중요하다. DIII-D 정상상태 하이브리드 실험 데이터베이스에서 찢어짐 모드 발생시의 플라즈마 전류 및 압력 분포의 특성은 찢어짐 모드가 발생한 위치에서의 국부적인 특성보다는 전체적인 분포 특성에 더 큰 영향을 받음을 확인할 수 있었다. 또한 찢어짐 모드가 발생한 위치에서의 플라즈마 저항성의 영향도 무시할 수 없음을 확인할 수 있었다.

찢어짐 안정성 지표 Δ' 는 재구성된 정확한 평형과 실험에서 측정한

플라즈마 분포를 이용하여 선형 고유값 해석 코드 (PEST-III, resistive DCON)를 통한 계산과 Rutherford 방정식을 이용한 추정으로 구해볼 수 있었다. 이렇게 구한 찢어짐 안정성 지표는 합리적인 수준에서의 일치함을 확인 및 검증할 수 있었다. 이때, 찢어짐 안정성 지표 Δ'의 값이 찢어짐 모드의 발생과 상관없이 양의 값을 가지는 것으로 나타났으며, 이를 통해 토로이달 장치에서 찢어짐 안정성의 임계 조건 $\Delta' > 0$이 충분조건이 아닐 수 있음을 추정해 볼 수 있었다.

선행연구에서 이론적으로 유도된 찢어짐 안정성 지표의 임계값을 도입하여 비교함으로써, 실험 평형에서 계산을 통해 구한 안정성 지표가 이론적인 찢어짐 안정성 지표의 임계값보다 클 때 ($\Delta' > \Delta'_c$) 찢어짐 모드가 불안정해지는 것을 확인할 수 있었다. 또한 NIMROD 코드를 이용한 찢어짐 모드의 크기 증가율 계산과 찢어짐 안정성 지표의 관계를 이용하여 찢어짐 안정성 지표의 임계값 Δ'_c를 추정할 수 있었다.

마지막으로, 기준 평형의 플라즈마 전류나 압력 분포의 국부적인 기울기 또는 플라즈마 특성을 대표하는 매개 변수를 합리적인 범위 내에서 변화시켜 새로운 평형을 재구성하고 분석함으로써, 실험에서 찢어짐 모드의 발생을 예측하기 위한 안정성 지표에의 의존성을 살펴보았다.

주요어 : 찢어짐 불안정성, 찢어짐 안정성 지표,
DIII-D 정상상태 하이브리드 시나리오, 안정성 도표

학 번 : 2011-30991